Scaling Laws of Quantum Information Lifetime in Monitored Quantum Dynamics

Bingzhi Zhang,[1,*] Fangjun Hu,[2] Runzhe Mo,[1] Tianyang Chen,[2] Hakan E. Türeci,[2] and Quntao Zhuang[1,3,†]

[1] *Ming Hsieh Department of Electrical and Computer Engineering, University of Southern California, Los Angeles, California 90089, USA*

[2] *Department of Electrical and Computer Engineering, Princeton University, Princeton, NJ 08544*

[3] *Department of Physics and Astronomy, University of Southern California, Los Angeles, California 90089, USA*

Quantum information is typically fragile under measurement and environmental coupling. Remarkably, we find that its lifetime can scale exponentially with system size when the environment is continuously monitored via mid-circuit measurements – regardless of bath size. Starting from a maximally entangled state with a reference, we analytically prove this exponential scaling for typical Haar random unitaries and confirm it through numerical simulations in both Haar-random and chaotic Hamiltonian systems. In the absence of bath monitoring, the lifetime exhibits a markedly different scaling: it grows at most linearly – or remains constant – with system size and decays inversely with bath size. We further extend our findings numerically to a broad class of initial states. We discuss implications for monitored quantum circuits in the weak measurement limit, quantum algorithms such as quantum diffusion models and quantum reservoir computing, and quantum communication. Finally, we evaluate the feasibility of resolving the predicted scaling regimes experimentally via noisy simulations of IBM Quantum hardwares.

I. INTRODUCTION

Quantum measurement is a defining feature of quantum mechanics – introducing irreducible randomness and collapsing superpositions in a way fundamentally distinct from unitary evolution. Beyond its foundational role, measurement has emerged as a powerful resource for engineering quantum states and probing the structure of many-body wavefunctions. In particular, mid-circuit measurements offer pathways for understanding thermalization in quantum systems, where subsystem measurements induce an emergent maximally random state ensemble in the complementary system [1, 2]. Monitored quantum circuit, a brickwork unitary circuit probabilistically doped with projective measurements, exhibits the measurement-induced phase transition (MIPT): as the measurement probability increases, a system can transition from volume-law to area-law entanglement [3, 4]. These results have resonated broadly, stimulating research across quantum information science, statistical mechanics, and condensed matter physics.

In the era of quantum science and engineering, a detailed understanding of the role of quantum measurement is essential for realizing quantum error correction [5], a cornerstone of fault-tolerant quantum computation. Experimental advances, particularly in superconducting qubit platforms, have demonstrated mid-circuit operations conditioned on measurement outcomes as a potential practical pathway toward scalable quantum computation [6]. Extending the lifetime of encoded quantum information in this setting requires carefully designed codes that preserve coherence in the logical quantum space during syndrome extraction. Mid-circuit measurement have also found utilities in quantum algorithms beyond error correction. To begin with, they enable the reuse of physical qubits as fresh ancillae, thereby reducing the physical resources in quantum computation. This approach has recently been demonstrated in the holographic deep thermalization protocol [7] and discussed for a range of other algorithms [8–14]. In these applications and beyond, the notion of quantum information lifetime plays an important role, and yet its connection to how mid-circuit measurement is performed is unclear, as we detail below.

In generative quantum models such as the Quantum Denoising Diffusion Probabilistic Model (QuDDPM) [15], of interest in the present work, mid-circuit measurement plays a central role. QuDDPM aims to learn a backward denoising process that maps a random state ensemble to the target ensemble, in a step-by-step fashion guided by a sequence of reference ensembles interpolating the target and initial ensembles, which are produced in a controlled forward scrambling process (see Fig. 1c). In each denoising step, mid-circuit measurement combined with a parameterized unitary is trained under a cost function. In this regard, mid-circuit measurement serves a dual role: it supplies intrinsic quantum randomness for generative learning and acts as a Maxwell's demon, denoising the system by steering transitions between quantum state ensembles. In this setting, the *quantum information lifetime* defined in this work serves as a proxy for the efficiency of state conversion and the rate of learning.

Quantum Reservoir Computing (QRC) [19, 20], a general-purpose quantum machine learning paradigm for processing time-dependent data, is another setting where the scaling behavior of quantum information lifetime is a key design consideration. An implementation of the QRC algorithm tailored for near-term quantum devices using mid-circuit measurements has been recently proposed and investigated [16, 17, 21–23]. In the noisy intermediate-scale QRC scheme (NISQRC) [17] analyzed

* bingzhiz@usc.edu
† qzhuang@usc.edu

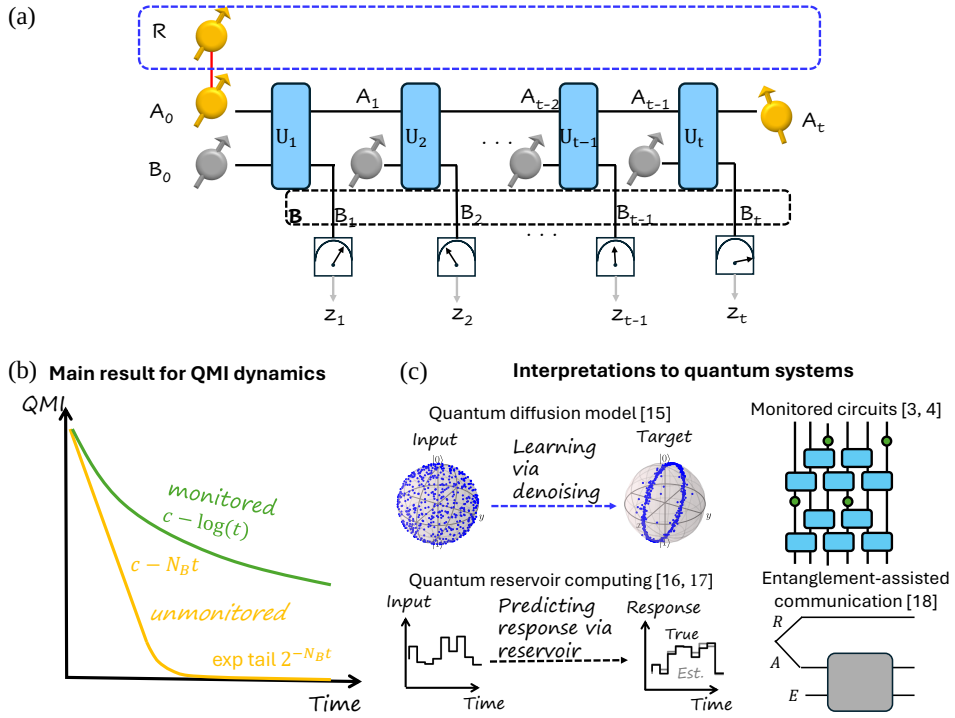

Figure 1. Schematic plot of quantum dynamics with mid-circuit measurement. In (a), initial input A_0 (N_A qubits) goes through interactions with bath via unitaries $U_1, U_2, \cdots, U_t$ to produce the final output A_t. Between each unitary, bath qubits B (N_B qubits) are measured and reset to $|0\rangle$'s in most of our discussions, except Section VII. Equivalently, one can regard the measurement as applied on bath qubits $B_1, B_2, \cdots, B_t$, each initialized in $|0\rangle^{\otimes N_B}$. To track the evolution of quantum information, we introduce the reference system R initially maximally entangled with A_0. The corresponding quantum mutual information (QMI) dynamics is sketched in (b), which decays which decays logarithmically or linearly in time with an exponential tail, depending on whether the bath is monitored or not. Panel (c) highlights connections between the model above and other models and algorithmic frameworks, including quantum denoising diffusion probabilistic model (QuDDPM) [15], quantum reservoir computing (QRC) [16, 17], monitored quantum circuits [3, 4], and entanglement-assisted communication [18]. The reference system surrounded by the blue dashed box in (a) indicates that it is not included in the original quantum circuit models except for communication setting.

here, a subset of qubits, designated as readout qubits, are repeatedly measured and reset as the data is streamed into the circuit, to approximate a target function of past inputs (see Fig. 1c). The remaining qubits, referred to as memory qubits, remain unmeasured. A key quantity of interest is the *memory time*, the ability of the system state to retain information about its past inputs [24, 25]. In reservoir computing, memory time plays a subtle role and must be carefully balanced with the non-linearity the system introduces on its inputs – a trade-off well-recognized in classical reservoir computing [26–28]. It is therefore important to understand the scaling of memory time – quantum information lifetime – with the measurement rate and system size.

In this work, we derive scaling laws for the quantum information lifetime in dynamical settings with and without bath monitoring enabled by mid-circuit measurements. When the system interacts with a periodically monitored bath and the measurement trajectory is recorded, the information lifetime can scale exponentially with the system size (in the context of NISQRC, this corresponds to the size of the memory subsystem). While without the monitoring – when the individual measurement trajectory is not recorded, the lifetime scales linearly or is a constant in system size. We establish our results analytically for typical unitaries using quantum mutual information between the system and a maximally entangled reference. These findings are supported by numerical simulations under both Haar-random and chaotic Hamiltonian dynamics across various initial states. For chaotic Hamiltonians, we identify atypical regimes where residual correlations persist for times that scale exponentially with system size. Our analysis highlights the importance of training in QuDDPM for achieving efficient generative learning. In the context of monitored quantum circuits studied for entanglement phase transitions, our results demonstrate an exponentially long quantum information lifetime in the weak measurement limit. We also interpret these results in the context of quantum reservoir computing, suggesting strategies for the design of the memory time in general dynamical systems. In the quantum communication setting, our results have implications for entanglement-assisted protocols, both with and without environment assistance. Finally, we propose

a hardware-friendly protocol for verifying mutual information dynamics through noisy simulations of the IBM Quantum hardware.

II. OVERVIEW

As depicted in Fig. 1a, we study a quantum circuit, where system A interacts unitarily with bath B in a repeated manner. In between each unitary, mid-circuit measurements are applied on the bath B. The central question we ask in this work is:

> *How does the initial quantum information in A decay through unitary evolution and mid-circuit measurements?*

To quantify the quantum information lost, we introduce a reference system R initially correlated with A_0 (see Fig. 1a). We adopt the quantum mutual information (QMI) between R and A_t as a measure to quantify the amount of quantum information in the system A_t for $t \geq 0$. The involvement of measurement means that access to measurement outcomes shapes the information dynamics, much like in the Wigner's friend scenario [29]. When the entire measurement trajectory is recorded, we refer to the bath as "monitored", indicating complete knowledge of the measurement dynamics. (Eq. (1)); conversely, lack of the full information of measurement trajectory decreases our knowledge about the final quantum state. In the extreme case, when the entire measurement trajectory is discarded, we regard the bath as being not monitored (Eq. (2)). Intermediate cases with partial measurement results recorded will be considered in future works. In this work, we examine the QMI dynamics under mid-circuit measurements with and without bath monitoring.

We analyze the QMI dynamics by first deriving analytical scaling expressions with respect to system size, assuming the R–A system starts in a maximally entangled Bell state. As sketched Fig. 1b, we prove that for typical monitored dynamics, the QMI vanishes logarithmically with time steps, leading to a lifetime that scales exponentially with system size, $\tau \sim 2^{N_A}$ and independent of bath size; while for typical unmonitored dynamics, the QMI decays linearly with time before entering a long-tail residual region, leading to a shorter lifetime with different scaling laws: $\tau \sim N_A/N_B$ or $\tau \sim 1/N_B$ depending on whether one focuses on the initial linear decay or the long-tail residual part. Our results are analytically established for typical dynamics under a maximally entangled initial state of the $R-A$ system and are further corroborated through numerical simulations of a broad class of correlated initial states.

Besides the typical cases represented by dynamics generated by Haar unitaries, we also examine atypical cases where dynamics generated by Hamiltonian dynamics without bath monitoring gives rise to a lifetime that scales exponentially.

Our results have implications in monitored quantum circuits, QuDDPM and QRC algorithms employing partial mid-circuit measurements, and entanglement-assisted communication as indicated in Fig. 1c. Our results show that monitored quantum circuits in the weak measurement limit support exponentially long quantum information lifetime. In terms of QuDDPM, our results indicate that training is essential for the efficient transport between two ensembles of quantum states — typical dynamics under random initialization preserves the structure of ensemble very well and therefore requires a large number of steps to complete the state transport. For mid-circuit-measurement-based QRC algorithms [16, 17, 21–23], our findings suggest that optimizing memory time for given resources may require going beyond the marginal distribution of measurements or employing non-generic Hamiltonian choices.

The paper is organized as follows. In Sec. III, we introduce the framework for information propagation in quantum dynamics with mid-circuit measurements, and the quantification of information lifetime. In Sec. IV, we present results for quantum information dynamics with a monitored bath. In Sec. V, we study the scenario without bath monitoring, including Haar unitary and anomalous Hamiltonian dynamics. We interpret our results in various scenarios in Sec. VI. In Sec. VII, we evaluate the effect of reset strategy on the information lifetime. In Sec. VIII, we examine the information dynamics from simulation of IBM quantum devices.

III. QUANTUM SYSTEM AND MUTUAL INFORMATION LIFETIME

A. Quantum circuit setup

We consider a general framework for quantum dynamics with mid-circuit measurements, as shown in Fig.1a. This framework underlies a broad class of algorithms including recent QRC algorithms [17, 30] and the QuDDPM [15]. The quantum system here consists of two subsystems: the data system A and the bath system B comprising N_A and N_B qubits respectively [31]. For the convenience of description, we also add a subscript t to A and B systems to denote the system at time step t. Starting from step $t = 0$, the data system A_0 takes an information-encoded quantum state, and the bath system B_0 is simply initialized in a trivial product state, e.g. $|\mathbf{0}\rangle \equiv |0\rangle^{\otimes N_B}$. At each time step t, the system undergoes a global unitary evolution U_t, which corresponds to either a chaotic evolution in the case of QRC or a parameterized quantum circuit in QuDDPM. This is followed by a projective measurement on the bath subsystem B_t, yielding a single-shot measurement outcome z_t. The resulting post-measurement state of the data subsystem A is then used as the input for the subsequent time step $t + 1$, where the process of unitary evolution and partial measurement is repeated. We first consider the

case in which the bath subsystem B is reset to the trivial product state $|\mathbf{0}\rangle_B$ at each time step. In Section VII, we demonstrate that this reset procedure does not affect our main conclusions regarding lifetime scaling.

For simplicity of description, we consider the reference and system to be initially in a pure state $|\Phi\rangle_{RA_0}$ for now. When the bath is monitored in each step, in t-th step, the Kraus operator applied on RA joint system corresponding to measurement outcome z_t on bath is $K_t = {}_{B_t}\langle z_t|(\boldsymbol{I}_R \otimes U_t)|\mathbf{0}\rangle_{B_{t-1}}$, therefore the final quantum state of RA_t conditioned on the measurement trajectory $\mathbf{z} = (z_1, \cdots, z_t)$ can be expressed as

$$|\psi_{\mathbf{z}}\rangle_{RA_t} = \frac{1}{\sqrt{P_{\boldsymbol{U}}(\mathbf{z})}} K_t \cdots K_2 K_1 |\Phi\rangle_{RA_0} \tag{1}$$

where $P_{\boldsymbol{U}}(\mathbf{z})$ is the probability of obtaining the measurement outcome $\mathbf{z}$.

Meanwhile, when the bath is not monitored, we also consider the dynamics of measurement-unconditioned quantum state. The unconditional state at step t is the state averaged over all measurement trajectories as

$$\rho_{RA_t} = \sum_{\mathbf{z}} P_{\boldsymbol{U}}(\mathbf{z}) |\psi_{\mathbf{z}}\rangle\langle\psi_{\mathbf{z}}|_{RA_t}. \tag{2}$$

Equivalently, one can regard the non-monitored bath being traced out in each time step. In this regard, the input-output relation from A_{t-1} to A_t, $\mathcal{P}_t(\cdot) = \mathrm{tr}_{B_t}\left[U_t\left(\cdot \otimes |\mathbf{0}\rangle\langle\mathbf{0}|_{B_{t-1}}\right)U_t^\dagger\right]$, defines the quantum channel $\mathcal{P}_t$. Therefore, the unconditional joint state can be described by the overall quantum channel

$$\rho_{RA_t} = \mathcal{I} \otimes (\mathcal{P}_t \circ \mathcal{P}_{t-1} \circ \cdots \mathcal{P}_1)(\rho_{RA_0}), \tag{3}$$

where $\mathcal{I}$ refers to the identity channel on the reference R.

B. Connecting to quantum models

Here we connect the quantum circuit dynamics under consideration to several different quantum models. The detailed interpretation can be found in Sec. VI.

The trajectory-conditional state from bath monitoring in Eq. (1) arises in the generative quantum machine learning models such as QuDDPM [15]. As shown in Fig. 1c, the goal of QuDDPM is to learn to sample a quantum state $|\phi\rangle$ from a certain distribution P_ϕ in a generative manner. The quantum circuit in Fig. 1a transports the initial random distribution towards the target distribution represented by the sample. Although the original QuDDPM does not require a reference system R, the dynamical transport of an ensemble of quantum states $\{\phi_k, P_{\phi_k}\}$ can be equivalently represented by the evolution of an entangled state between a reference R and system A, $|\psi\rangle_{RA} = \sum_k \sqrt{P_{\phi_k}} |k\rangle_R |\phi_k\rangle_A$, where $|k\rangle$ is an orthonormal bases to denote the sample index. The induced quantum state ensemble structure change can generally be captured by the change in the quantum correlation between reference R and A_t.

On the other hand, the dynamics of the unconditional state in Eq. (3) provides insight to the current approaches of QRC [17, 19, 20, 30]. QRC aims to learn a complex functional mapping from a sequence of classical data to an output classical data sequence. Ref. [17] highlights the importance of balancing memory time and nonlinearity in QRC, using a Volterra-series-based analysis, and argues that the memory time should align with the timescale of the target learning task. In the NISQRC implementation, classical data is encoded into the quantum system via parametric unitaries $U_1, \cdots, U_t$ in Fig. 1a and the output features are obtained from marginal distributions $P(z_1), \cdots P(z_t)$ of the measurement results (see details in Sec. VI B), with dynamics characterized by Eq. (3). Although the original NISQRC framework does not involve a reference system R, introducing a classical-quantum (CQ) state over RA provides an equivalent description of classical data input into the quantum system A (for details, see Section VI B. Therefore, memory time of classical input can be captured by the correlation between R and A_t, in the unconditional state in Eq. (3).

In the monitored circuit where a brickwork unitary circuit is probabilistically doped with projective measurements, as shown in Fig. 1c, both trajectory-conditional and unconditional states can be studied. Our model considered in Fig. 1a can be regarded as a toy model of monitored circuits, where the entire system is always fully scrambled between each round of subsystem projective measurements on a fixed number of N_B qubits. Due to the fully scrambling unitary, we can fix the N_B measured qubits as the bath and the rest as the system. While the entanglement dynamics is well-studied, the loss of quantum information due to measurement is unclear. To capture the quantum information, we can therefore introduce the reference system R initially entangled with the data qubits A. In this context, the conditional state in Eq. (1) refers to the resulting state in a particular experiment, while Eq. (2) corresponds to the average state without post-selection.

The quantum circuit can also be interpreted in the scenario of entanglement-assisted communication through the channel $\mathcal{P}_t \circ \cdots \mathcal{P}_1$ specified in Eq. (3). In this case, the reference system R provides the entanglement assistance in communication and the QMI quantity directly corresponds to entanglement-assisted communication capacity [18]. The case without environment assistance corresponds to the unmonitored dynamics described in Eq. (3). On the other hand, for monitored dynamics, in each experiment, the receiver will not only receive the conditional state $|\psi_{\mathbf{z}}\rangle_{RA_t}$ in Eq. (1), but as well as the measurement trajectory $\mathbf{z}$, which is a classical message about the environment bath status, therefore, we can interpret the monitored dynamics as environment-assisted communication.

In all applications, we introduce the reference system R to facilitate the study of the quantum information dy-

namics. While the size of the reference system R varies according to the application scenario, in this work we consider R to be the same size with system A, which includes cases of $|R| < |A|$ when the correlation between R and A is not maximal.

C. Quantum mutual information lifetime

Taking into account the measurement-conditioned state $|\psi_{\mathbf{z}}\rangle_{RA_t}$ and unconditioned state ρ_{RA_t} at time step t, we quantify the information shared by parties R and A_t via QMI. Given a measurement trajectory $\mathbf{z}$, the quantum information retained in A_t at time step t is quantified by the *measurement-conditioned QMI* defined as:

$$\overline{I(R:A_t|\mathbf{z})} \equiv \mathbb{E}_{\mathbf{z}}\, I(R:A_t|\mathbf{z}), \tag{4}$$

where $\mathbb{E}_{\mathbf{z}}$ denotes averaging over the different measurement outcomes according to the outcome probabilities $P_{\boldsymbol{U}}(\mathbf{z})$, and $I(R:A_t|\mathbf{z})$ is the QMI of the conditional state $|\psi_{\mathbf{z}}\rangle_{RA_t}$ in Eq. (1). For the unconditional dynamics, the *measurement-unconditioned QMI*

$$I(R:A_t) \equiv S(\rho_R) + S(\rho_{A_t}) - S(\rho_{RA_t}), \tag{5}$$

is thus evaluated on ρ_{RA_t} in Eq. (3), where ρ_R, ρ_{A_t} are the reduced states on corresponding subsystem R, A_t.

The differing order of QMI evaluation and the ensemble average $\mathbb{E}_{\mathbf{z}}$ in the measurement-conditioned and unconditioned QMI reflects distinct physical scenarios. The measurement-conditioned QMI (Eq.(4)) captures the information retained in a typical conditional state $|\psi_{\mathbf{z}}\rangle$ obtained from the corresponding measurement trajectory. In contrast, the unconditioned QMI is computed from the averaged state ρ_{RA_t}, which contains no information about any measurement outcome (see Eq.(2)). We further interpret the measurement-conditioned and unconditioned QMI introduced above in the setting of entanglement-assisted communication, as detailed in Section VI D.

In both cases of monitored and unmonitored circuits, to quantify the preservation of quantum information, we define the ϵ-lifetime τ_{cond} and τ_{uncond} of quantum information via the decay of QMI by

$$\text{QMI}|_{t=\tau} = \epsilon \times \text{QMI}|_{t=0}, \tag{6}$$

where QMI can be either $\overline{I(R:A_t|\mathbf{z})}$ or $I(R:A_t)$ for conditional and unconditional QMI, and $\epsilon < 1$ is a free constant. Specifically, with Bell state as the initial state, the quantum communication capability measured by the coherent information $I(R\rangle A_t)$ starts with unity and decays to zero at the half-life of QMI (i.e. $\epsilon = 1/2$) in unmonitored dynamics, as detailed in Section VI D.

To study the generic properties of quantum dynamics, we model each of the unitary U_k as a fixed unitary sampled from Haar ensemble. This is a good approximation, e.g. when the quantum dynamics is chaotic or a deep random quantum circuit. To characterize the typical case, we consider the Haar ensemble averaged conditional (unconditional) QMI.

To provide a concrete example, we also consider the Hamiltonian dynamics $U = e^{-iHt_H}$ generated by an all-to-all coupled Ising Hamiltonian [17] through a relatively long time $t_H \gg 1$

$$H = \sum_{i<j} J_{ij}\sigma_j^z\sigma_j^z + \sum_{i=1}^{L}\eta_i^x\sigma^x + \sum_{i=1}^{L}\eta_i^z\sigma_i^z, \tag{7}$$

where the coupling strength $J_{i,j}$, transverse x-field strength η_i^x and longitudinal z-drive η_i^z are randomly chosen, i.e. standard normal distributed (zero mean and unit variance). All unitaries $U_k = U = e^{-iHt_H}$ is identical throughout the various time steps ($t_H = 50$ is chosen throughout the paper). Our numerical results, summarized in Appendix B indicate that our conclusions remain valid regardless of whether the same unitary is used at each time step or different unitaries are chosen independently.

IV. EXPONENTIAL QMI LIFETIME IN MONITORED DYNAMICS

With the framework for information propagation in place, we now examine the dynamics of quantum information under mid-circuit measurements and resets, focusing on the measurement-conditioned QMI in Eq. (4) proposed for monitored dynamics. To begin with, we consider the maximally entangled state, $|\Phi\rangle_{RA_0} \propto \sum_j |j\rangle_R |j\rangle_{A_0}$, to obtain analytical results; Then, we numerically extend the analytical results with less-entangled states, perturbed Haar random states and classical-quantum (CQ) hybrid states. We define the perturbed Haar random states as $|\phi^\delta\rangle_{RA_0} \propto |\phi_{\text{Haar}}\rangle_{RA_0} + \delta\,|\mathbf{0}\rangle_{RA_0}$. Similarly, we define the family of CQ states to be $(\rho^\delta)_{RA_0} \propto \sum |j\rangle\langle j|_R \otimes \left|u_j^\delta\right\rangle\!\left\langle u_j^\delta\right|_{A_0}$ with perturbed basis $|u_j^\delta\rangle_{A_0} \propto |u_j\rangle_{A_0} + \delta\,|\mathbf{0}\rangle_{A_0}$, where $|u_j\rangle$ forms an orthonormal basis. In both cases, δ interpolates highly correlated ($\delta = 0$) and uncorrelated states ($\delta \gg 1$). Throughout the paper, we take the number of reference qubits equaling N_A for simplicity.

Using Haar random unitaries to model the chaotic evolution, we have the following theorem, where $d_A = 2^{N_A}, d_B = 2^{N_B}$ are dimension of data and bath Hilbert spaces (see Appendix D for proof).

Theorem 1 *The expected measurement-conditioned mutual information of an initial Bell state in quantum dynamics with mid-circuit measurements and reset at time*

t is asymptotically ($d_A \gg 1$) lower bounded by

$$\mathbb{E}_{\text{Haar}}\,\overline{I(R:A_t|\mathbf{z})}$$
$$\gtrsim 2(2t+1)N_A + 2tN_B - 2\log_2\left[(d_A d_B+1)^t (d_A+1)^{t+1}\right]$$
$$- 2\log_2\left[\left(\frac{d_A d_B-1}{d_A d_B+1}\right)^t - \left(\frac{d_A-1}{d_A+1}\right)^{t+1}\right] + 2 \qquad (8)$$
$$\simeq 2N_A - 2\log_2\left[(1-1/d_B)t+1\right]. \qquad (9)$$

In the large bath limit of $d_B \gg 1$, the dynamics of QMI converges to a universal form $\mathbb{E}_{\text{Haar}}\,\overline{I(R:A_t|\mathbf{z})} \gtrsim 2N_A - 2\log_2(t+1)$. We can estimate the ϵ-lifetime for measurement-conditioned QMI as

$$\tau_{\text{cond}} \gtrsim \frac{d_B}{d_B-1}\left(2^{(1-\epsilon)N_A}-1\right) \sim \Omega(\exp(N_A)), \qquad (10)$$

which grows exponentially with the data system size N_A and independent of bath system size once $d_B \gg 1$.

Fig. 2a shows numerical simulations of the measurement-conditioned QMI dynamics in the model where each step we apply a random unitary sampled from Haar ensemble (dark blue dots), and its decay behavior versus time steps is well characterized by our theoretical lower bound (red dashed) in Eq. (9) as long as the bound remains positive. The gap between theoretical lower bound and numerical simulation arises from the difference between Rényi-2 and von Neumann entropies, detailed in Appendix F. The relatively small sample fluctuation shown by the error bars further indicates that the Haar average result can represent the dynamics with a typical implementation of $\boldsymbol{U}$. Moreover, the numerical results for dynamics of $\overline{I(R:A_t|\mathbf{z})}$ utilizing a fixed Hamiltonian evolution in each step (light blue dots) also closely aligns with Haar results, thus indicating a wide applicability of our theory to different types of quantum dynamics. In Fig. 2b, we interpret the QMI dynamics via the lifetime, and similar agreement between the Haar dynamics (blue dots), Hamiltonian dynamics (cyan dots) and the prediction (red dashed) from Eq. (9) can be found, confirming the exponential scaling of the lifetime with system size N_A.

Besides the initial Bell state, we also numerically extend the results to the QMI dynamics of various other initial quantum states, including the perturbed Haar states and CQ states, presented in Fig. 2c and d. To compare with Theorem 1, we plot with the QMI normalized by the initial value $I(R:A_0)$ as the y-axis and take a logarithmic scale x-axis with a rescaled time $(1-1/d_B)t+1$ indicated by Eq. (9). As shown in Fig. 2c and d, the prediction of Theorem 1 appears linear in such a rescaling (red dashed). Indeed, the results for various quantum states (green curves) align with the Bell state result (blue solid) and demonstrate an agreement with the theory prediction (red dashed).

As the lower bound Eq. (8) (or the simplified version Eq. (9)) becomes negative at extremely late time, we expect deviations from the lower bound. Indeed, in Fig. 2c and d we see the curves deviate from the red dashed lower bound curve. In Appendix C, we study this deviation numerically and identify an exponentially decaying tail of QMI. Taking the late-time states as the initial states, we show that such a decay still supports a lifetime exponential in N_A because of the exponentially suppressed exponent of the tail.

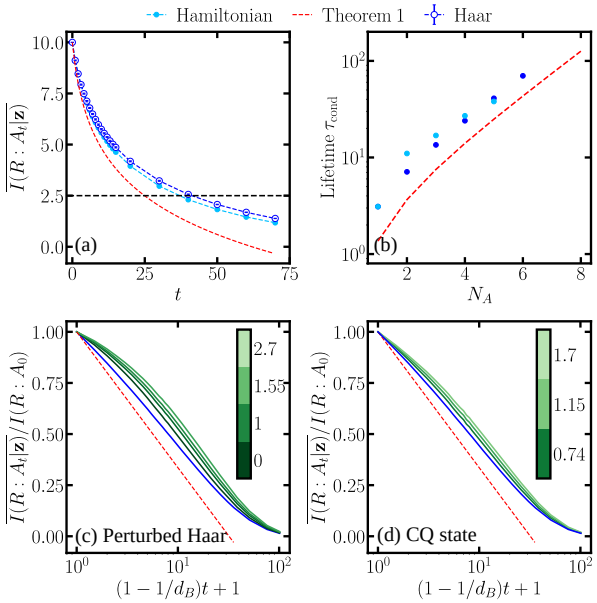

Figure 2. Measurement-conditioned QMI $\overline{I(R:A_t|\mathbf{z})}$ in monitored dynamics with reset. In (a) we plot numerical simulation results of (von Neumann entropy version) $\overline{I(R:A_t|\mathbf{z})}$ with random Haar unitary (dark blue dots) and fixed Ising Hamiltonian evolution (light blue dots) in a system of $N_A = 5, N_B = 1$ qubits. Errorbars represent sample fluctuations of Haar unitary implementations. Red dashed line represents the theoretical asymptotic lower bound of Eq. (9) in Theorem 1. Horizontal black dashed line indicate the threshold of $\overline{I(R:A_t|\mathbf{z})} = \overline{I(R:A_0|\mathbf{z})}/4$. In (b), we show the growth of lifetime versus data system N_A for numerical simulation results of Haar and Hamiltonian unitary implementation. Red dashed line represent the theoretical result in Eq. (10) with $\epsilon = 1/4$. In (c) and (d), we plot decay of normalized QMI in numerical simulations with initial states of perturbed Haar states ϕ_δ and CQ states ρ_δ versus a shifted time separately. Blue lines are Bell states result with Haar unitary in (a) for reference. The color bar shows the value of δ.

V. QMI LIFETIME IN UNMONITORED DYNAMICS

In this section, we study the unmonitored dynamics where the measurement trajectory of bath is not recorded during the dynamics described by Eq. (3).

A. Linear and constant lifetime for typical unitary

To characterize the decay of quantum information in the unmonitored scenario, we analyze the QMI of the unconditional state defined in Eq. (5). As in the monitored case, we begin with a maximally entangled Bell state to facilitate analytical calculations. For computational convenience, we adopt a Rényi version of mutual information $I_2(R:A_t)$ defined by replacing the von Neumann entropy in Eq. (5) with Rényi-2 entropies. Although this extension may not satisfy all property requirement of QMI, we numerically find that it fits well with the dynamics of the actual QMI. Indeed, for special classes of quantum states, Rényi-2 based QMI well captures quantum correlation [32] and agrees well with von Neumann based QMI [33], which is also utilized in the experiment of MIPT [34]. With regard to the dynamics of Rényi extended mutual information, we thus have the following theorem (see Appendix E for a proof).

Theorem 2 *The expected Rényi-2 extended measurement-unconditioned QMI of a Bell initial state in the quantum dynamics of 2-design unitaries with mid-circuit measurements and reset at time t is*

$$\begin{aligned}&\mathbb{E}_{\text{Haar}}\, I_2(R:A_t)\\ &\simeq \log_2\left(\frac{\left(d_A^2-1\right)d_B\left(\frac{\left(d_A^2-1\right)d_B}{d_A^2d_B^2-1}\right)^t+d_B+1}{d_A^2d_B+1}\right)\\ &\quad-\log_2\left(\frac{d_A^2(d_B+1)-\left(d_A^2-1\right)\left(\frac{\left(d_A^2-1\right)d_B}{d_A^2d_B^2-1}\right)^t}{d_A^3d_B+d_A}\right)+N_A.\end{aligned} \tag{11}$$

In the asymptotic limit $d_A, d_B \gg 1$, when $t \ll 2N_A/N_B$,

$$\mathbb{E}_{\text{Haar}}\, I_2(R:A_t) \simeq 2N_A - tN_B, \tag{12}$$

while for $t \gg 2N_A/N_B$,

$$\mathbb{E}_{\text{Haar}}\, I_2(R:A_t) \simeq d_A^2 d_B^{-t}. \tag{13}$$

At early time, Eq. (12) indicates a linear decay of quantum information; while at late time, Eq. (13) indicates an exponential decay of quantum information.

The late-time exponential decay of QMI in Eq. (13) can be also explained from a quantum channel spectrum approach [17], which holds for general initial states. Here, we focus on the case where the same unitary is applied repeatedly, and therefore $\mathcal{P}_k = \mathcal{P}$ for all time steps $1 \le k \le t$. Consider the spectrum of the channel defined as the following: $\mathcal{P}\sigma_\alpha = \lambda_\alpha \sigma_\alpha$, where we regard the quantum operators as vectors, e.g., expanded in the Pauli basis. Note that σ_α's are generally not quantum states. The largest eigenvalue corresponds to the fixed point state of the channel, $\lambda_0 = 1$ and $\sigma_0 = \rho_{\text{fix}}$ satisfying $\mathcal{P}\rho_{\text{fix}} = \rho_{\text{fix}}$. The second largest eigenvalues (in terms of the norm) generally come in conjugate pairs $\{\lambda_1, \lambda_1^*\}$, with corresponding operator representation of eigenvector $\{\sigma_1, \sigma_1^\dagger\}$ given the real matrix representation of channel $\mathcal{P}$. For the initial state ρ_{RA_0}, we can in general decompose it as

$$\rho_{RA_0} = \sum_{i,j} c_{ij}\gamma_i \otimes \sigma_j = \sum_j o_j \otimes \sigma_j, \tag{14}$$

where γ_j forms a basis of operators on reference system R and $o_j = \sum_i c_{ij}\gamma_i$ are operators. Note that o_j's are generally not valid quantum states. Applying the channels $\mathcal{P}$ for $t \gg 1$ times following the unmonitored dynamics in Eq. (3), we have

$$\rho_{RA_t} = \sum_j o_j \otimes \lambda_j^t \sigma_j \tag{15}$$

$$\simeq o_0 \otimes \rho_{\text{fix}} + \lambda_1^t o_1 \otimes \sigma_1 + \lambda_1^{*t} o_1^\dagger \otimes \sigma_1^\dagger. \tag{16}$$

As QMI is continuous in the quantum states, from Taylor expansion the QMI

$$I(R:A_t) \propto |\lambda_1|^{ct} \tag{17}$$

where c is a positive integer.

For Haar random unitary induced channel $\mathcal{P}$, all eigenvalues filling a disk of radius $1/\sqrt{d_B}$ except for λ_0 [35] (see Fig. 3g). Therefore, we have $I(R:A_t) \propto d_B^{-ct}$, which recovers the prediction from Theorem 2.

In Fig. 3a, we verify the predictions in Theorem 2 for Bell state, finding the close agreement between QMI of numerics (dots) and Rényi-2 extended QMI of theory (lines). The QMI indeed has a linear decay for both the Haar unitary dynamics and the Hamiltonian dynamics, when the environment is not monitored; in the late time region, we also observe an exponential decay (see Fig. 3b). The Hamiltonian dynamics also shows similar behavior, except that the late time decay exponent is different from the theory prediction, which we will explore in detail in Section V B. In Fig. 3c-f, we further extend the numerical simulation to less correlated initial states, including various perturbed Haar random states and CQ states. Both the early time linear decay and late-time exponential decay are observed.

With Theorem 2 and its generalizations established, we anticipate that the scaling behavior of QMI dynamics can vary depending on the choice of initial state, as explained below.

1. *Linear lifetime for typical cases*

For typical states of interest, the dynamics is dominated by the linear decay and we can obtain the unmonitored ϵ-lifetime from Eq. (12) as

$$\tau_{\text{uncond}} \simeq 2(1-\epsilon)N_A/N_B. \tag{18}$$

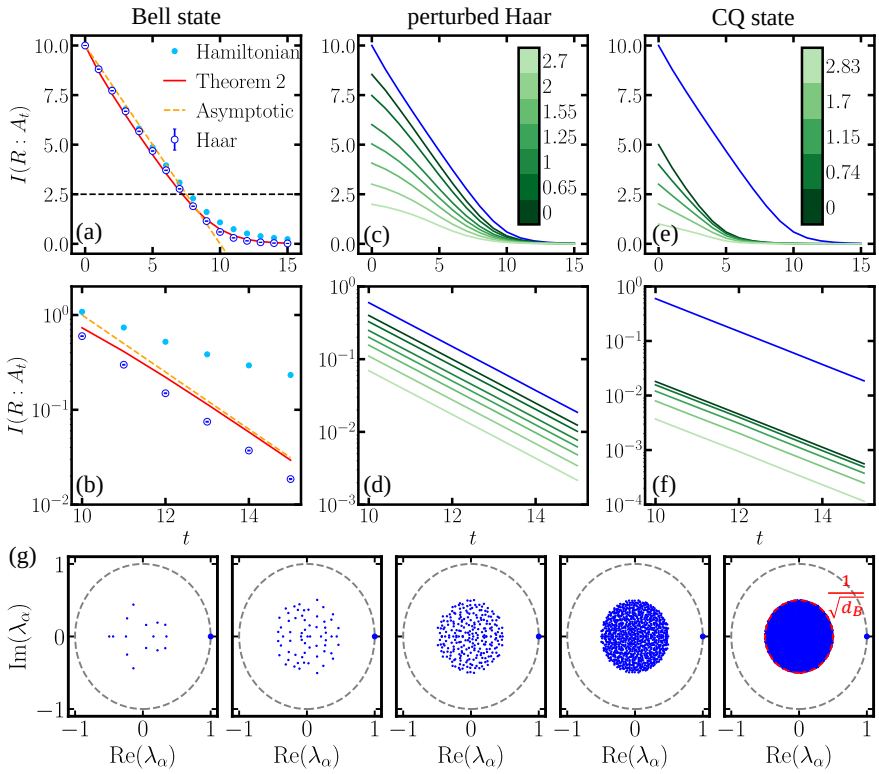

Figure 3. Measurement-unconditioned QMI $I(R:A_t)$ in unmonitored dynamics with reset. In (a) we plot numerical simulation results of $I(R:A_t)$ of a Bell initial state with random Haar unitary (dark blue dots) and fixed Ising Hamiltonian evolution (light blue dots) in a system of $N_A = 5, N_B = 1$ qubits. Errorbars represent sample fluctuations of Haar unitary implementations. Red and orange lines represent the exact and asymptotic theory of Eq. (11) and Eq. (12) in Theorem 2. Horizontal black dashed line indicate the threshold of $\epsilon = 1/4$. Late-time dynamics is presented in (b) with orange line showing asymptotic theory of Eq. (13) in Theorem 2. In (c) and (e), we plot numerical simulation of $I(R:A_t)$ under Haar unitary dynamics with initial perturbed Haar states and CQ states separately. Dark to light green lines represent different perturbation δ indicated by the colorbar. Blue lines represent Haar result from (a) for reference. In both cases, we have 5 reference and data qubits. (d) and (f) are corresponding late-time dynamics, and blue lines is Haar result from (b). In (g), we show the eigen-spectrum of $\mathcal{P}$ implemented by Haar unitary from $N_A = 2$ to 6 (from left to right) with $N_B = 2$ bath qubits. The red dashed circle indicates the radius of $1/\sqrt{d_B}$.

Interestingly, the lifetime without monitoring the bath agrees with the notion of "thermalization time" in *holographic deep thermalization* [7] which scales $\sim N_A/N_B$ though with a factor of 2 difference due to Bell initial state. On the contrary, the lifetime of Eq. (10) with bath monitoring reveals a different time-scale of information lost toward equilibrium. In Fig. 4a, we verify the linear QMI lifetime of Bell initial state for both Haar unitary and Hamiltonian evolution. Moreover, through our observations in Fig. 3c and e, we expect that the linear lifetime holds for other types of typical states as we considered there.

2. *Constant lifetime for residual dynamics*

For certain states with extremely low correlation, the late time dynamics of Eq. (13) dominates. This happens for initial states whose expansion in Eq. (16) becomes precise even at an early time. Since Eq. (13) indicates an exponential decay at the rate of d_B^{-t}, lifetime defined in Eq. (6) with time zero shifted to late time leads to

$$\tau_{\text{uncond}} \simeq \log_2(1/\epsilon)/N_B, \tag{19}$$

a constant independent of data system size. In the inset (Fig. 4b1), we do see a collapse of exponential QMI decay with increasing system size N_A, when we adopt the initial state from the late-time ($t \gg 2N_A/N_B$) unconditional state (Eq. (2)) evolved from a Bell state $|\Phi\rangle_{RA_0}$. For such weakly correlated states, QMI lifetime does not depend on system size as shown in Fig. 4b.

B. Anomaly in Hamiltonian dynamics: exponential lifetime from outliers

Figure 3b shows that, under the dynamics generated by the Hamiltonian in Eq. (7), the exponent governing

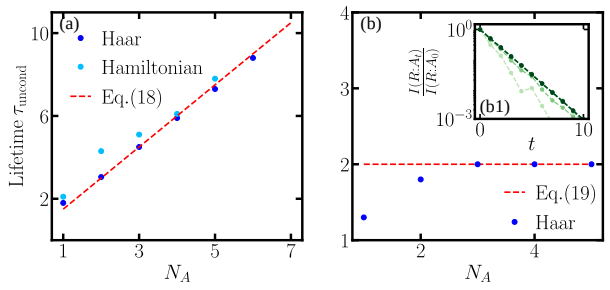

Figure 4. Lifetime of measurement-unconitioned QMI $I(R:A_t)$ in unmonitored dynamics with reset. In (a), we show QMI lifetime versus system size N_A with Bell initial state for Haar (blue) and Hamiltonian (cyan) unitary implementation. Red dashed line represents the theoretical result in Eq. (18). In (b), we show QMI lifetime for Haar unitary with initial state ρ_{RA_0} to be unconditional state in dynamics with Bell initial state at late-time. Red dashed line represents theory in Eq. (19). Inset shows the decay of normalized QMI with $N_A = 1$ to 5 (light to dark). In both cases, we take $\epsilon = 1/4$.

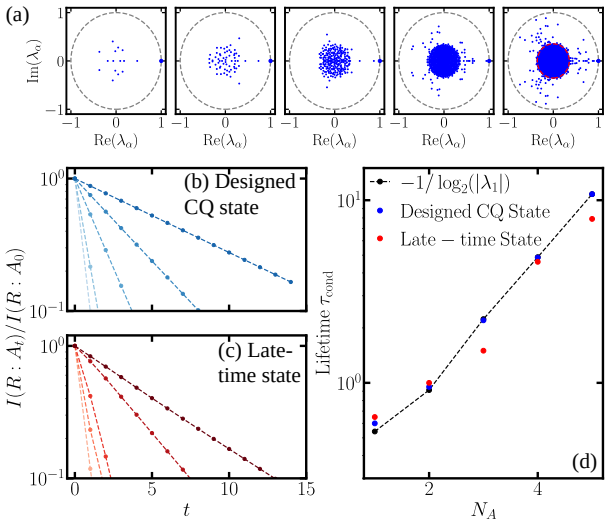

Figure 5. Measurement-unconditioned QMI in unmonitored Hamiltonian dynamics with reset. In (a), we show the eigenspectrum of channel $\mathcal{P}_0$ from $N_A = 2$ to 6 (left to right). Red dashed circle indicates the radius of $1/\sqrt{d_B}$. In left bottom panel, we plot the decay of normalized QMI in different system size with initial state ρ_{RA_0} to be (b) the designed CQ state in Eq. (20) and (c) unconditional state in dynamics with Bell initial state at late-time separately. Colored lines from light to dark represent system size of $N_A = 1$ to 5. In (d), we show their corresponding lifetime and compare to the memory time τ_{eig}. In all cases, we fix bath size $N_B = 3$.

the exponential decay of the QMI is significantly smaller than the theoretical prediction given in Theorem 2, indicating a notable deviation from Haar dynamics. In the following, we examine this anomaly in detail.

For the late-time dynamics, Eq. (17), derived using the quantum channel spectrum approach, remains generally applicable. Therefore, we start with an analysis based on the spectrum of the Hamiltonian-induced quantum channel. In Fig. 5a, we numerically find that for the Hamiltonian evolution considered, most eigenvalues concentrate within a constant-size disk of size $1/\sqrt{d_B}$ (red dashed circle) for increasing system size N_A, similar to the Haar case in Fig. 3g. However, there exist isolated eigenvalues located between the bulk of the spectrum and the fixed point eigenvalue $\lambda_0 = 1$. These outliers contribute to the residual information retained in the system and serve as a phenomenological analog, in the channel spectrum, to the eigenstate spectrum observed in the "many-body scar" Hamiltonian [36]. We note that the Hamiltonian in Eq. (7) does not feature a low-entanglement energy tower, which is a one of the key hallmarks of many-body scarred systems. As a result, we find that the theoretical memory time, given by $\tau_{\text{eig}} = -1/\log_2(|\lambda_1|)$, deviates from the Haar prediction and instead exhibits exponential growth with N_A, as indicated by the green dots in Fig. 5d.

As an example, we can construct a classically correlated state between the reference and memory system as

$$\rho_{RA_0} = \frac{1}{2}\left[|0\rangle\langle 0| \otimes \rho_{\text{fix}} + |1\rangle\langle 1| \otimes \left(\rho_{\text{fix}} + a(\sigma_1 + \sigma_1^\dagger)\right)\right], \tag{20}$$

for a properly chosen a such that $\rho_{\text{fix}} + a(\sigma_1 + \sigma_1^\dagger)$ is a valid quantum state. Here ρ_{fix} and σ_1 are the eigenvectors of the Hamiltonian induced quantum channel $\mathcal{P}$. Iterating the dynamics with channel $\mathcal{P}$ in Eq. (3) to time step t, we have

$$\rho_{RA_t} = \frac{1}{2}\left[|0\rangle\langle 0| \otimes \rho_{\text{fix}} + |1\rangle\langle 1| \otimes \left(\rho_{\text{fix}} + a\lambda_1^t\sigma_1 + a\lambda_1^{*t}\sigma_1^\dagger\right)\right]. \tag{21}$$

which is a special case of Eq. (16). Therefore, we can infer the lifetime as in Eq. (17) with $|\lambda_1|$ following exponentially scaling as we have seen. We see that the choice of initial state in Eq. (20) guarantees the dominance of the first non-unity eigenvalue λ_1 in Eq. (16) even at early time. Therefore, the QMI decays exponentially at early time, as confirmed in Fig. 5b.

Besides the designed CQ state, we numerically evaluate the QMI with initial state from late-time ($t \gg 2N_A/N_B$) unconditional state evolved from a Bell state under the Hamiltonian dynamics in Fig. 5c. In contrast to the collapsed behavior in the inset of Fig. 4b1, QMI decays exponentially at different rates with increasing system size N_A. Figure 5d clearly shows an exponential increase in the QMI lifetime, consistent with the scaling of the memory time $\tau_{\text{eig}} = -1/\log_2(|\lambda_1|)$ discussed above.

VI. INTERPRETATION IN QUANTUM CIRCUIT MODELS

Having completed the analysis of QMI lifetime, we now apply the framework introduced in Sec. III to interpret

our results within the context of quantum computing models, monitored quantum circuits and entanglement-assisted communication.

A. Quantum diffusion models

In quantum diffusion models, i.e. QuDDPM [15], we aims to learn the distribution of a target state ensemble, and generate new samples following this distribution, referred to as the quantum generative learning (see Fig. 1c). In the forward process of QuDDPM, the states samples from the target state ensemble are evolved with controllable scrambling unitaries to approach the Haar random states ensemble. The forward process stands as a reference dynamical process for the learning in backward process. In the backward learning process, the data and bath system are initially prepared in a random state and a trivial product state. Here we introduce the reference system to index the states on the data system for analysis convenience. In particular for the state ensemble $\{|\phi_k\rangle, P_{\phi_k}\}_k$, it can be equivalently represented as

$$|\psi\rangle_{RA} = \sum_k \sqrt{P_{\phi_k}} |k\rangle_R |\phi_k\rangle_A . \tag{22}$$

In the t-th step, the joint system of data and bath evolves through a parameterized unitary $U_t(\boldsymbol{\theta}_t)$ followed by mid-circuit measurements on the bath system. Ideally, we expect the output state ensemble in t-th step to match the corresponding state ensemble in the forward process, and as the backward denoising process proceeds, the final output state ensemble from backward circuits follows the same distribution of the target states ensemble of interest. As the output state depends on the whole measurement trajectory, the backward learning process refers to the monitored dynamics studied in Sec. IV.

According to our theoretical results in Theorem 1, in the backward denoising process, if we simply apply unitary circuits with randomly initialized parameters, it at least requires exponential number of steps to erase the correlation between the reference index system and the states in the data system, which makes the denoising process inefficient and hard for near-term devices and applications. This negative insight thus highlights the importance of training. When we compare the output state ensemble of backward circuits and forward scrambling, minimizing a well-designed loss function can guide us to optimize the parameterized unitary $U_t(\boldsymbol{\theta}_t)$, which stores the information for mapping from input state ensemble from the prior step in backward process toward the output ensemble in corresponding forward step, therefore boosts the backward learning process in reducing the number of steps.

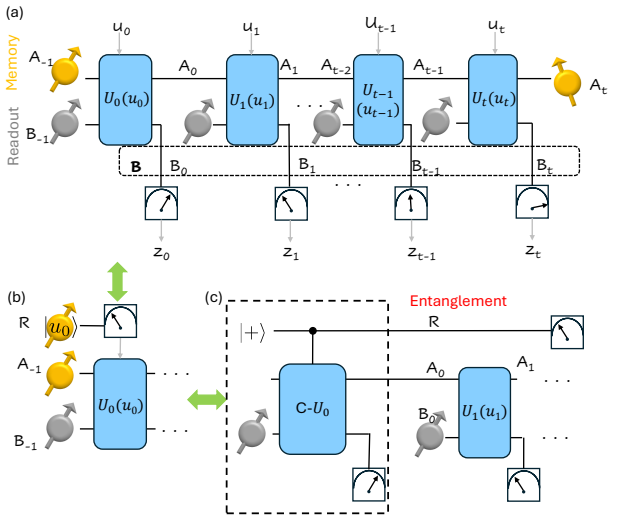

Figure 6. Reduction from the reservoir computing paradigm with classical inputs $u_0 u_1 \cdots u_t$ to the quantum circuit with entangled input RA_0.

B. Quantum reservoir computing

The objective of QRC is to learn a functional that maps a temporal sequence $\boldsymbol{u} = \{\cdots, u_0, u_1, \cdots, u_t, \cdots\}$ to an output sequence $\boldsymbol{y}$. In a mid-circuit-measurement based QRC setup [17, 23], the system consists of a memory and readout register with N_A and N_B qubits, respectively. The system undergoes a sequence of unitary evolutions $U_t(u_t)$, conditioned on the classical input u_t (see Fig. 6a). In typical implementations of $U_t(u_t)$, the unitary, for instance, can be generated by a parameterized Hamiltonian $H + u_t \sum_{i=1}^{L} \eta_i^z \sigma_i^z$ with H defined in Eq. (7).

After implementing each unitary, one measures the readout system to obtain results $\{\cdots, z_0, z_1, \cdots, z_t, \cdots\}$, each $z_t \in \{0,1\}^{N_B}$ is a binary bitstring. Through repetitions of experiments, one can obtain the learning features $\boldsymbol{x}(t)$, a normalized 2^{N_B}-dimensional vector of unconditional measurement statistics of $z_t \in \{0,1\}^{N_B}$, with each component being the probability of the corresponding measurement outcome z_t. For example, with $N_B = 3$ readout qubits, $x_7(t) = \text{Prob}[z_t = 111]$. The final output y_t is estimated as a weighted sum: $y_t = \boldsymbol{w} \cdot \boldsymbol{x}(t)$.

Consider the dynamics that starts with unitary $U_0(u_0)$ encoded with the classical input u_0, as shown in Fig. 6b, one can equivalently introduce a reference system R, whose quantum state $|u_0\rangle$ determines the dynamics of the memory-readout system $A_{-1}B_{-1}$ via a measurement: one measures R in the encoding bases $\{|u_0\rangle\langle u_0|\}$ and then performs the unitary $U_0(u_0)$ conditioned on the measurement result. Taking a step further in Fig. 6c, one can consider R in a superposition state $|+\rangle \propto \sum_{u_0} |u_0\rangle$ assuming equal prior probability of u_0 without losing generality and the measurement-conditioned unitary is realized as a control-unitary gate defined as $\text{C} - U_0 = \sum_{u_0} |u_0\rangle\langle u_0|_R \otimes U_0(u_0)$. In this regard, assuming ini-

tial trivial product state, the $RA_{-1}B_{-1}$ system becomes entangled via the control unitary, and after the first measurement on the readout system, the state RA_0 remains entangled while B_0 is reset to $|\mathbf{0}\rangle_{B_0}$, leading to a reduction towards the set-up in Fig. 1a. Since our theoretical analysis assumes typical and sufficiently complex unitary dynamics $U_1, \ldots, U_t$, we can neglect the subsequent inputs $u_1, \ldots, u_t$ when focusing on the memory of the initial input u_0, following the same reasoning as in Ref. [17].

In this context, the fading memory effect in reservoir computing can be quantified by the correlation between the initial input u_0 and the readout z_t, as a function of the time step t. Since QRC employs marginal measurement statistics to compute $y_t = \boldsymbol{w} \cdot \boldsymbol{x}(t)$, all relevant information is contained within the unconditional quantum state described in Eq. (3). Consequently, the correlation between u_0 and z_t can be characterized by the unconditional classical mutual information $I^{\mathrm{C}}(u_0 : z_t)$, which is upper bounded by the quantum mutual information in Eq. (5), as dictated by the data processing inequality.

By initializing the system in a Bell state on RA_0, the linear-in-system-size lifetime of the unconditional QMI dynamics discussed in Sec. V A also implies a corresponding memory time linear in the size of the memory subsystem of QRC, assuming sufficient complex unitary dynamics. For Hamiltonian dynamics, on the other hand, the structure of Hamiltonian considered supports exponential lifetime in system size, as we recognize in Sec. V B when tailoring the correlation to spectrum structure. However, such a specific weak initial correlation requires the input u_0 to affect the dynamics in a specific form and may not be utilized in a specific learning task. Overall, the general framework to interpret information loss in QRC is also applicable to recent advances in feedback-driven QRC with appropriate modifications [19].

To make use of more information from measurements, we propose to utilize a longer sequence of the memory outcome in multiple consecutive steps, instead of a single step. Let's begin with an extreme case, where at each step one adopts the full measurement outcome history $\mathbf{z}_t = (z_1, z_2, \cdots, z_t)$ in learning the approximation of the function. Considering the $N_B t$ total number of qubits measured, the measurement statistics of $\boldsymbol{z}$ defines the feature $\boldsymbol{x}(t) = \{x_0(t), \cdots, x_{2^{N_B t}-1}(t)\}$, i.e. the probability of the measurement outcomes, and output can be estimated by $y_t = \boldsymbol{w} \cdot \boldsymbol{x}(t)$. Note that such an extended scheme includes the case of adopting only the distribution of measurement result z_t from the t-th step, via choosing a weight to reproduce the output only from marginal distribution. Consider the case of $t = 2$ as an example, $\boldsymbol{z} \in \{00, 01, 10, 11\}$ and $\boldsymbol{x}(2) = \{x_{00}, x_{01}, x_{10}, x_{11}\}$, by limiting the weight to be $\boldsymbol{w} = (w_0, w_1, w_0, w_1)$, the output using the whole $\boldsymbol{x}(2)$ then becomes $y_2 = w_0(x_{00} + x_{10}) + w_1(x_{01} + x_{11})$, which matches the output from marginal distribution at $t = 2$.

Apparently, now y_t is derived from the statistics of the entire trajectory and the mutual information between y_t and u_0 is upper bounded by

$$I^C(u_0 : y_t) \leq I^C(u_0 : \mathbf{z}_t). \tag{23}$$

In this case, memory time is maximal as the early measurement result z_1 always appears in any y_t as expected. However, we can ask how much additional information, ΔI^C_{t+1}, does the additional measurement z_{t+1} provides about u_0, to provide insight on whether increasing t can assist in the learning of u_0. Taking the upper bound as an estimation, we have

$$\Delta I^C_{t+1} \equiv I^C(u_0 : \{z_1, \cdots, z_t, z_{t+1}\}) - I^C(u_0 : \{z_1, \cdots, z_t\}) \tag{24}$$

$$= I^C(u_0 : z_{t+1} | \{z_1, \cdots, z_t\}) \equiv I^C(u_0 : z_{t+1} | \mathbf{z}_t). \tag{25}$$

In this case, the additional correlation between z_{t+1} and u_0 can be described by the classical conditional mutual information $I^C(u_0 : z_{t+1}|\mathbf{z})$, as previous measurement outcomes are taking into account in the learning. Adopting data processing inequality in each trajectory of $\mathbf{z}_t$, we have $I^C(u_0 : z_{t+1}|\mathbf{z}_t) \leq I(R : A_t|\mathbf{z}_{t-1})$. Accordingly, results in Sec. IV indicates a slow logarithmic decay and therefore the additional information is appreciable for an exponentially long time.

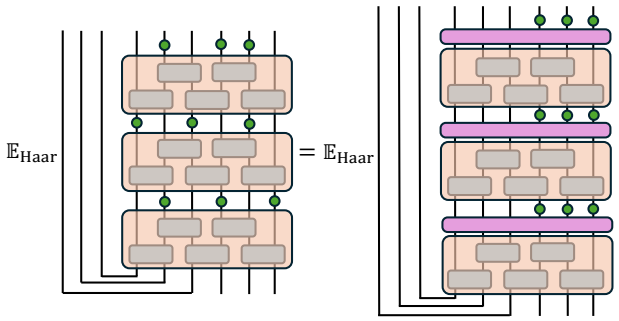

Figure 7. Equivalence of the monitored quantum circuit in the weak measurement limit (left) and the monitored circuit in the weak measurement limit with fixed qubits to be measured (right). Purple rectangles represent permutation operators.

C. Monitored quantum circuits

In the monitored quantum circuit set-up, a brickwork-style unitary circuit is applied onto a trivial product initial state, with projective measurements randomly performed on qubits following every layers of unitary gates at a chosen probability q. Recent studies [3, 4] have shown that with the increasing measurement probability q, the bipartite entanglement entropy of the resulting state transits from volume-law to area-law, known as the measurement-induced phase transition (MIPT). The model we considered in Fig. 1a can be regarded

as a toy model of monitored circuits in the weak measurement limit, where the data and bath system are always fully scrambled between each time of projective measurements. In addition, instead of measuring each qubit with a certain probability, we fix the number of qubits to be measured as N_B among the $N_A + N_B$ qubits. For typical Haar random unitary with exponential complexity [37], the equivalent measurement probability $q \sim N_B/(N_A + N_B)\exp(N_A + N_B)$ can be exponentially small; therefore, our model can be regarded as the monitored circuit in the weak-measurement limit and the output state follows volume-law entanglement for any cut within the data system.

With the extension of the monitored circuit, initial information stored in a local system, i.e. the data system, propagates across the whole system via random unitary circuit, and gets lost due to the projective measurements. We focus on the information remained in the unmeasured subsystem through the dynamical process of monitored circuit in the weak measurement limit. To keep track of the initial information in the local subsystem, we introduce the same reference system that is maximally entangled with the data system. In the weak measurement limit, given that the unitary circuit between every two layers of measurements is sufficient complex (Fig. 7 left), we are allowed to insert an extra layer of permutation operation (purple) to rearrange the position of measured and unmeasured qubits in the system while without changing the ensemble average result (see Fig. 7 right). With this equivalence transformation, the measurement-conditioned QMI $\overline{I(R:A_t|\mathbf{z})}$ defined in Eq. (4) characterizes the typical amount of information remained in the unmeasured system, and according to our theoretical result of Theorem 1 in Sec. IV, the quantum information initially stored in a local subsystem can persist in the quantum system for exponentially long time through monitored circuits in the weak measurement limit. However, if we do not keep the record on the measurement outcome trajectory in the experiment, the quantum information can only persist in a linearly long time following Theorem 2 in Sec. V.

D. Entanglement-assisted communication

To close this section, we interpret our results in the entanglement-assisted communication setting. While we focus on classical messages, quantum messages are equivalent at half of the communication rate due to quantum teleportation [18].

Let's begin with the measurement-unconditioned QMI in Eq. (5). As shown in Fig. 8 top, the unmonitored dynamics naturally fits into the setup of entanglement-assisted communication [18]. The sender aims to send a classical message via the input A_0 towards the quantum channel $\mathcal{I}_R \otimes \boldsymbol{\mathcal{P}}$ with $\boldsymbol{\mathcal{P}} = \mathcal{P}_t \circ \cdots \circ \mathcal{P}_1$. Following the definition of channel $\mathcal{P}$ of Eq. (3), we can represent the channel $\boldsymbol{\mathcal{P}}$ via a unitary $V = \prod_{\ell=1}^{t} U_\ell$ applied on the

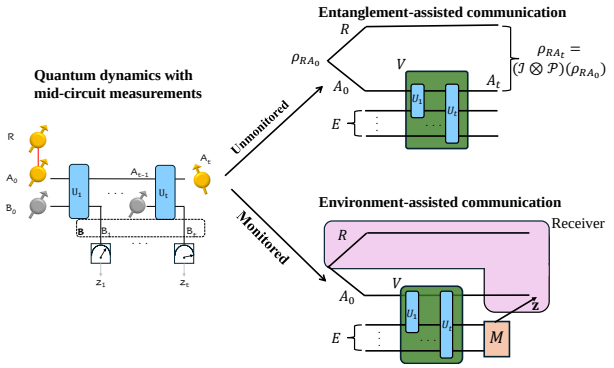

Figure 8. Connection from quantum dynamics with mid-circuit measurements in unmonitored and monitored cases to entanglement-assisted communication without (top) and with (bottom) environment assistance.

sender A_0 and environment $E = B_0 \cdots B_{t-1}$ which is a joint system of expanded baths initialized in $|0^{\otimes N_B t}\rangle_E$. A reference system R to purify the input A_0 is sent through the identity channel as the entangled ancilla, which is required by definition of the communication setup and different from the cases discussed above. The entanglement-assisted classical capacity of the channel $\boldsymbol{\mathcal{P}}$ quantifies the maximum bit transmission rate provided the shared entanglement, is known as [18]

$$C_E(\boldsymbol{\mathcal{P}}) = \max_{\rho_{A_0}} S(\rho_{A_0}) + S(\boldsymbol{\mathcal{P}}(\rho_{A_0})) - S\left((\mathcal{I}\otimes\boldsymbol{\mathcal{P}})\,|\Phi\rangle\langle\Phi|_{RA_0}\right) \tag{26}$$

$$= \max_{\rho_{A_0}} S(\rho_R) + S(\rho_{A_t}) - S\left(\rho_{RA_t}\right) \tag{27}$$

$$= \max_{\rho_{A_0}} I(R:A_t), \tag{28}$$

where in the second line we utilize the fact that R purifies A_0. Therefore, our results on the unmonitored dynamics in Theorem 2 provides an achievable lower bound on the entanglement-assisted capacity as Bell state input is one of the possible input states. Similarly, in *noisy super-dense coding*, the unconditional QMI $I(R:A_t)$ quantifies the amount of classical bits to be sent provided a shared entangled state ρ_{RA_t} [38].

Next, we connect the measurement-conditioned QMI defined by Eq. (4) in the scenario of environment-assisted classical communication. We still follow the setup of noisy super-dense coding, where Alice applied a quantum channel $\boldsymbol{\mathcal{P}}$ to her side and send it to Bob, who owns the other side R entangled with A_0 and A_t at the end to recover the information sent from Alice, shown by the pink shaded area. However, unlike the earlier unconditional case, now at the output side of environment Charlie performs measurement M and transmits the measurement outcome $\mathbf{z}$ to the receiver A_t via classical communication. In each time conditioned on the measurement outcome $\mathbf{z}$, the maximum information Bob can learn about Alice's information is the QMI of state $|\psi_{\mathbf{z}}\rangle_{RA_t}$, therefore the measurement-conditioned QMI $\overline{I(R:A_t|\mathbf{z})}$ represents an

achievable rate of communication *on average case*, and the logarithmic decay of conditional QMI in Theorem 1 indicates a large advantage in communication rate due to the assistance of classical information from environment.

Besides the entanglement-assisted communication scenario, we can further consider a connection to quantum communication. As $S(\rho_R)$ remains a time-dependent constant in our set-up (for instance $S(\rho_R) = N_A$ for Bell-state input), the decay of unconditional QMI in fact reveals the dynamics of coherent information

$$I(R\rangle A_t) \equiv S(\rho_{A_t}) - S(\rho_{RA_t}) \tag{29}$$
$$= I(R:A_t) - S(\rho_R). \tag{30}$$

Following our definition of QMI lifetime in Eq. (6), for a given initial input state ρ_{RA_0}, there always exists a threshold above which a positive quantum communication from R to A_t can be realized. The threshold corresponds to $I(R\rangle A_t) = I(R:A_t) - S(\rho_R) = 0$, and since from Eq. (6) we define $I(R:A_t) = \epsilon I(R:A_0)$, we have the threshold value $\epsilon = S(\rho_R)/I(R:A_0)$. Specifically, for a pure entangled state $|\Phi\rangle_{RA_0}$, we have $\epsilon = 1/2$.

VII. EFFECT OF RESET STRATEGY

Up to this point, our analysis has focused on the quantum dynamics with mid-circuit measurements followed by a reset operation, which erases any prior information in the bath and reinitializes it to a trivial state – e.g., $|0\rangle^{\otimes N_B}$ – for the next time step. In contrast, without the reset strategy, the measurement outcome z_t of the bath system is retained and used as the initial state for the subsequent step, i.e., $|z_t\rangle$.

For the measurement-conditioned QMI $\overline{I(R:A_t|\mathbf{z})}$, we can directly prove that the with/without reset strategy does not make a difference in the dynamics of QMI (see proof in Appendix. A), which can be understood by the invariance of integrand changing in the Haar integral. We verify the conclusion through numerical simulations for the logarithmic decay in Fig. 9a (see verification on the residual dynamics in Appendix. C).

In contrast, for the measurement-unconditioned QMI dynamics, the reset strategy makes a difference in the measurement-unconditioned information dynamics. Due to the lack of knowledge about previous measurement results, the input state of bath system to the next step equivalently becomes a diagonal classical state $\rho'_{B_t} = \sum_{z_t} P(z_t)\,|z_t\rangle\langle z_t|$, therefore we can treat the operation without reset as a mapping toward classical-quantum state via a dephasing channel. To obtain analytical understanding on the information dynamics, we instead consider another strategy by resetting the input state of bath system to fully-mixed state $\boldsymbol{I}_B/d_B$ which is expected to provide the fastest decay in information dynamics due to its maximal classical Shannon entropy [39], and it also corresponds to the infinite-temperature thermal state. We expect the results with fully-mixed state reset to capture the one *without* reset at late time. This is because in the dynamics without reset, the repeated measurement and random unitaries will converge the unconditional bath state towards the fully mixed state at late time, up to finite-size correction. We have the following theorem (see Appendix E for a proof).

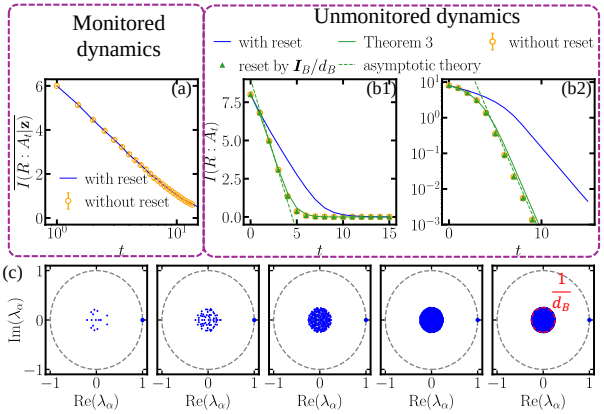

Figure 9. QMI dynamics in monitored / unmonitored dynamics with different reset strategy. In (a), we plot decay of measurement-conditioned QMI with reset (blue) and without reset (orange). In (b1) and (b2), we plot numerical simulation of measurement-unconditioned QMI with (blue) and without (orange) reset strategy in early and late time separately. Green triangles show the numerical result of reset by fully mixed state. Green solid lines show the theory of Eq. (31) in Theorem 3; Green dashed lines in (b1) and (b2) show the corresponding asymptotic theory of Eq. (32) and Eq. (13). Errorbars represent sample fluctuations of Haar unitary implementations without reset. The system consists of (a) $N_A = 3$ and (b1-b2) $N_A = 4$ data qubits, and $N_B = 1$ bath qubits. In (c), we show the spectrum of Haar channel with fully mixed state reset of system size from $N_A = 2$ to 6 (left to right) with $N_B = 2$ bath qubits. The red dashed circle indicates the radius of $1/d_B$.

Theorem 3 *The expected Rényi-2 extended measurement-unconditioned QMI of a Bell initial state in the quantum dynamics of 2-design unitaries with mid-circuit measurements and fully-mixed state reset at time t is*

$$\mathbb{E}_{\text{Haar}}\, I_2(R:A_t)$$
$$\simeq \log_2\left(\left(d_B - \frac{1}{d_A^2}\right)\left(\frac{d_A^2-1}{d_A^2 d_B^2-1}\right)^t + \frac{1}{d_A^2}\right)$$
$$- \log_2\left(\frac{d_B-1}{d_A}\left(\frac{d_A^2-1}{d_A^2 d_B^2-1}\right)^t + \frac{1}{d_A}\right) + N_A. \tag{31}$$

In the asymptotic limit $d_A, d_B \gg 1$, when $t \ll N_A/N_B + 1/2$,

$$\mathbb{E}_{\text{Haar}}\, I_2(R:A_t) \simeq 2N_A + N_B - 2N_B t, \tag{32}$$

while for $t \gg N_A/N_B + 1/2$,

$$\mathbb{E}_{\text{Haar}}\, I_2(R:A_t) \simeq d_A^2 d_B^{1-2t}. \tag{33}$$

Compared to Theorem 2, the information dynamics in both early and late time still exhibits a corresponding linear / exponential decay, but at a decrease rate twice larger. This factor-of-two difference coincides with the fact that the Bell state purification of a fully mixed state requires a dimension of the bath system of d_B^2, if one wants to interpret the purified bath system as the overall bath in the case of reset to pure states.

Accordingly, the ϵ-lifetime is estimated as

$$\tau_{\text{uncond}} \simeq \begin{cases} (1-\epsilon)\,(N_A/N_B+1/2)\,, & t \ll N_A/N_B+1/2, \\ \log_2(1/\epsilon)/2N_B, & t \gg N_A/N_B+1/2. \end{cases} \tag{34}$$

which is only approximately half of the corresponding lifetime compared to the one with zero state reset strategy in Eq. (18) and Eq. (19).

Through numerical simulation with Haar unitaries (see Fig. 9b1 and b2), the measurement-unconditioned QMI dynamics without bath reset strategy (orange dot) surprisingly agrees well with the one with fully-mixed state reset (green triangles), which overlaps with our theory prediction in Theorem 3, thus demonstrate the double-speed linear and exponential decay compared to zero state reset strategy (blue line) in early and late stage. Moreover, the eigenspectrum of channel with Haar unitary and fully mixed state reset strategy concentrates in a disk of radius $1/d_B$ [35], shown in Fig. 9c, providing supports to the intuition and theorem proposed above. Since the quantum channel in the absence of reset is unital – which maps identity to identity – the fixed point associated with $\lambda_0 = 1$ is the fully mixed state. In quantum reservoir computing, such a unitality property yields a memoryless system under the long-time limit [17], and the memory fading rate depends on $|\lambda_1|$. Due to the intrinsic chaotic property of Hamiltonian dynamics considered here, we expect that the reset strategy would lead to similar scaling laws. Meanwhile, the anomaly case of QMI lifetime in Hamiltonian dynamics without the reset strategy remains unexplored, and we leave it as an interesting open question.

VIII. SIMULATION OF QMI DYNAMICS ON NEAR-TERM HARDWARE

In this section, we validate the exponential separation in measurement-conditioned and unconditioned QMI dynamics through near-term hardware compatible realizations. With a focus on the superconducting platform of IBM Quantum devices, we implement the fast scrambling ansatz (FSA) [40] to mimic the implementation of Haar random unitary in theoretical modeling of Fig. 1a with appropriate modifications to reduce circuit compilation cost (see Appendix. G). We perform both ideal and noisy simulations of IBM quantum devices via Qiskit [41]. For the IBM Quantum Sherbrooke we targeted at, it has median T_1 as $275.73\mu s$, median echoed cross-resonance (ECR) gate error 7.726×10^{-3}, median SX error 2.300×10^{-4}, median ECR gate length $5.333 \times 10^{-1}\mu s$, median readout (measurement) length $1.216\mu s$, thus our simulation of 15 steps is within the coherence time of qubits, which is also support by the conditional state purity $\gtrsim 0.75$ with details in Appendix. G.

In Fig. 10a, we evaluate the QMI dynamics implemented with FSA. For the ideal simulation, both measurement-conditioned (light blue dots) and unconditioned (light green dots) QMI align with the simulation results with Haar unitaries (solid lines), demonstrating its scrambling ability to mimic the dynamics with random unitaries. Next, we adopt the noisy circuit model (excluding measurement error) from Qiskit and simulate the QMI dynamics. In the presence of hardware noises, both conditioned (dark blue) and unconditioned (dark green) QMI show the same scaling of dynamics though with a small deviation from the ideal results. We thus expect that the exponential separation of QMI lifetime in conditional versus unconditional setup can be robust against circuit noise, suggesting a practical advantage on current-generation hardware.

The above simulation results on the dynamics of QMI replies on a complete tomography of quantum states. In practice, one could consider the alternatives based on Rényi entropy [34]. However, for Rényi entropy estimation via the randomized measurement, there still exists a statistical error factor of $1/\sqrt{M}$ for applying M sets of measurement unitaries due to central limit theorem, and a large number of shots are still required for each choice of measurement unitaries [42]. To mitigate the resource cost for practical applications, inspired by the cross-entropy benchmark for verifying MIPT [43], we propose a quantum-to-classical (Q2C) mutual information protocol. Through the same dynamics as in Fig. 1a, we define the measurement-conditioned Q2C mutual information as

$$\begin{aligned} &\overline{I^{\text{Q2C}}(R:A_t|\mathbf{z})} \\ &\equiv \mathbb{E}_{\mathbf{z}}\, D_{\text{KL}}(P_{\boldsymbol{U}|\mathbf{z}}(z_R,z_{A_t})||P_{\boldsymbol{U}|\mathbf{z}}(z_R)\otimes P_{\boldsymbol{U}|\mathbf{z}}(z_{A_t})), \end{aligned} \tag{35}$$

where $P_{\boldsymbol{U}|\mathbf{z}}(z_R) = |_R\langle z_R|\psi_{\mathbf{z}}\rangle_{RA_t}|^2$ is the marginal distribution of measurement result on subsystem R and similar for $P_{\boldsymbol{U}|\mathbf{z}}(z_{A_t})$, while $P_{\boldsymbol{U}}(z_R,z_{A_t}) = |\langle z_R,z_{A_t}|\psi_{\mathbf{z}}\rangle_{RA_t}|^2$ is the corresponding joint distribution of (z_R,z_{A_t}) on the conditional state $|\psi_{\mathbf{z}}\rangle_{RA_t}$ (see definition in Eq. (1)), and D_{KL} is the KL divergence. In the same spirit, we can also define the measurement-unconditioned Q2C mutual information as

$$I^{\text{Q2C}}(R:A_t) \equiv D_{\text{KL}}(P_{\boldsymbol{U}}(z_R,z_{A_t})||P_{\boldsymbol{U}}(z_R)\otimes P_{\boldsymbol{U}}(z_{A_t})), \tag{36}$$

with marginal and joint distributions measured on the unconditional state ρ_{RA_t} defined in Eq. (2), i.e. $P_{\boldsymbol{U}}(z_R) = \text{tr}(\rho_{RA_t}|z_R\rangle\langle z_R|_R)$ and $P_{\boldsymbol{U}}(z_R,z_{A_t}) = \text{tr}\big(\rho_{RA_t}|z_R,z_{A_t}\rangle\langle z_R,z_{A_t}|_{RA_t}\big)$.

Through the conversion of quantum correlation to state measurement outcome statistics, we only need to perform computational basis measurement in the Q2C

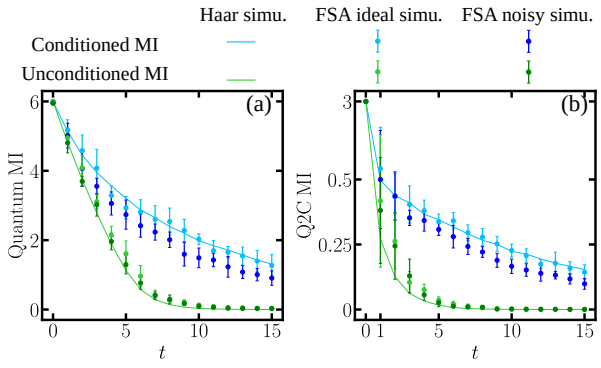

Figure 10. Dynamics of measurement-conditioned and unconditioned (a) QMI and (b) Q2C MI. Solid lines represent Haar simulation results. Dark and light colored dots with errorbars represent ideal and noisy simulation results separately with fast scrambling ansatz (FSA) for IBM Quantum, Sherbrooke. Here we perform simulation on a system of $N_A = 3, N_B = 1$ qubits with FSA consisting of $L = 2$ layers, and 1024 shots for mid-circuit measurements on the bath system. Each dot is averaged over 10 randomized circuits.

protocol without any extra quantum operation which significantly reduces the sample complexity. The measurement results $\{(z_R, z_{A_t}, \mathbf{z})\}$ with $\mathbf{z}$ to be the measurement trajectory of bath can be further utilized to estimate all statistics involved in Eqs. (35) and (36). This protocol can save more resources in running quantum devices following the spirit of *"measure first, ask questions later"* [44] though at the cost of losing characterization of quantum information partially through the quantum to classical conversion. We leave an in-depth analysis of complexity and statistical error as future studies.

In Fig. 10b, we simulate the Q2C mutual information dynamics with FSA. Similar to the behavior of the QMI dynamics discussed above, the measurement-conditioned Q2C mutual information (blue) also decays logarithmically with steps, while the unconditioned one (green) simply decays linearly, and both of them present a small deviation in the noisy simulation, therefore the Q2C protocol is a well-defined quantity for witness of the exponential separation in mutual information lifetime on near-term devices with hardware resource reduction in experiments.

IX. DISCUSSION

In this work, we demonstrate that quantum information can exhibit a lifetime that scales exponentially with system size, even in the presence of interactions with an arbitrary environment, provided the environment (bath) is monitored at each time step. In contrast, when the environment is left unmonitored, we show that the lifetime of quantum information – such as that stored in a Bell state – scales only linearly with system size.

In the case of Hamiltonian dynamics, we observe an anomalously long exponential lifetime of classical correlations. This behavior is attributed to Hamiltonian-dependent outliers in the spectrum of the corresponding single-step quantum channel – a phenomenon whose precise origin remains an intriguing open question from the perspective of quantum many-body physics.

We further demonstrate the exponential separation in QMI dynamics through the noisy simulation of IBM Quantum devices, propose a Q2C mutual information protocol for hardware-efficient witness of this separation and test it.

Our QMI framework provides a useful perspective for understanding memory dynamics in mid-circuit-measurement-based QRC algorithms. We propose extending memory time by leveraging statistics from sequences of measurement outcomes. This approach holds potential for improved performance, warranting further investigation through detailed numerical and experimental studies.

Our results also offer valuable insights for the field of quantum machine learning, including applications such as quantum diffusion models and quantum reservoir computing. For generative quantum machine learning models such as QuDDPM that incorporate recorded mid-circuit measurements, our theoretical result on the exponentially long QMI lifetime reveals a limitation: efficient learning of the transformation from random initial states to a target ensemble is challenging for chaotic circuits with high representation power Consequently, careful design and training of relatively shallow circuits at each denoising step of QuDDPM are essential for enabling effective state ensemble learning. Additionally, the linear lifetime of mutual information in unmonitored dynamics offers guidance for setting the appropriate temporal window in QRC when learning individual signals. Incorporating statistics from extended sequences of measurement outcomes may further enhance the ability to learn non-Markovian sequences. Finally, our findings provide theoretical support for the security of holographic deep thermalization against entanglement attacks, as identified in Ref. [7].

We point out some future directions. The robustness of the exponential separation in quantum information lifetime against various types of noise is interesting to explore for both theoretical understanding and practical applications on near-term devices. It remains an open question whether the change in QMI dynamics – from logarithmic decay in monitored systems to linear decay in unmonitored ones – can be understood as a dynamical phase transition with a corresponding interpretation in statistical physics. For practical experimental verification, a statistical analysis of the proposed Q2C mutual information is useful for uncovering both its strengths and limitations. Another experimental direction for demonstrating QMI dynamics is to design a reliable witness of the exponential separation in QMI behavior that avoids post-selection, thereby reducing the required resources. An intriguing question is whether the decay of QMI ob-

served in this work can be linked to local system thermalization and the emergent state design in holographic deep thermalization [7].

ACKNOWLEDGMENTS

QZ, BZ and RM acknowledge support from NSF (CCF-2240641, OMA-2326746, 2350153), ONR N00014-23-1-2296, AFOSR MURI FA9550-24-1-0349 and DARPA (HR0011-24-9-0362, HR00112490453, D24AC00153-02). This work was partially funded by an unrestricted gift from Google. HET, FH and TC acknowledge support from the DARPA contract HR00112190072, AFOSR award FA9550-20-1-0177, and AFOSR MURI award FA9550-22-1-0203. The views, opinions, and findings expressed are solely the authors' and not the U.S. government's. The writing of the manuscript is completed in part at Aspen Center for Physics, which is supported by National Science Foundation grant PHY-2210452

[1] W. W. Ho and S. Choi, Phys. Rev. Lett. **128**, 060601 (2022).
[2] J. S. Cotler, D. K. Mark, H.-Y. Huang, F. Hernandez, J. Choi, A. L. Shaw, M. Endres, and S. Choi, PRX quantum **4**, 010311 (2023).
[3] Y. Li, X. Chen, and M. P. Fisher, Phys. Rev. B **100**, 134306 (2019).
[4] B. Skinner, J. Ruhman, and A. Nahum, Phys. Rev. X **9**, 031009 (2019).
[5] A. R. Calderbank and P. W. Shor, Phys. Rev. A **54**, 1098 (1996).
[6] Google Quantum AI and Collaborators, Nature **638**, 920 (2025).
[7] B. Zhang, P. Xu, X. Chen, and Q. Zhuang, arXiv:2411.03587 (2024).
[8] A. D. Córcoles, M. Takita, K. Inoue, S. Lekuch, Z. K. Minev, J. M. Chow, and J. M. Gambetta, Phys. Rev. Lett. **127**, 100501 (2021).
[9] M. DeCross, E. Chertkov, M. Kohagen, and M. Foss-Feig, Phys. Rev. X **13**, 041057 (2023).
[10] E. Bäumer, V. Tripathi, D. S. Wang, P. Rall, E. H. Chen, S. Majumder, A. Seif, and Z. K. Minev, PRX Quantum **5**, 030339 (2024).
[11] L. Piroli, G. Styliaris, and J. I. Cirac, Phys. Rev. Lett. **133**, 230401 (2024).
[12] H. Buhrman, M. Folkertsma, B. Loff, and N. M. Neumann, Quantum **8**, 1552 (2024).
[13] K. C. Smith, A. Khan, B. K. Clark, S. Girvin, and T.-C. Wei, PRX Quantum **5**, 030344 (2024).
[14] M. Iqbal, N. Tantivasadakarn, R. Verresen, S. L. Campbell, J. M. Dreiling, C. Figgatt, J. P. Gaebler, J. Johansen, M. Mills, S. A. Moses, *et al.*, Nature **626**, 505 (2024).
[15] B. Zhang, P. Xu, X. Chen, and Q. Zhuang, Phys. Rev. Lett. **132**, 100602 (2024).
[16] J. Chen, H. I. Nurdin, and N. Yamamoto, Physical Review Applied **14**, 024065 (2020).
[17] F. Hu, S. A. Khan, N. T. Bronn, G. Angelatos, G. E. Rowlands, G. J. Ribeill, and H. E. Türeci, Nat. Commun. **15**, 7491 (2024).
[18] C. H. Bennett, P. W. Shor, J. A. Smolin, and A. V. Thapliyal, IEEE Trans. Inf. Theo. **48**, 2637 (2002).
[19] K. Nakajima, K. Fujii, M. Negoro, K. Mitarai, and M. Kitagawa, Phys. Rev. Applied **11**, 034021 (2019).
[20] K. Fujii and K. Nakajima, Phys. Rev. Applied **8**, 024030 (2017).
[21] P. Mujal, R. Martínez-Peña, G. L. Giorgi, M. C. Soriano, and R. Zambrini, npj Quantum Information **9**, 16 (2023).
[22] T. Yasuda, Y. Suzuki, T. Kubota, K. Nakajima, Q. Gao, W. Zhang, S. Shimono, H. I. Nurdin, and N. Yamamoto, arXiv:2310.06706 [quant-ph] (2023).
[23] R. Martínez-Peña and J.-P. Ortega, Physical Review E **107**, 035306 (2023).
[24] H. Jaeger, GMD-German National Research Institute for Computer Science (2002) (2002).
[25] S. Ganguli, D. Huh, and H. Sompolinsky, Proceedings of the National Academy of Sciences **105**, 18970–18975 (2008).
[26] J. Dambre, D. Verstraeten, B. Schrauwen, and S. Massar, Scientific Reports **2**, 514 (2012).
[27] D. Verstraeten, J. Dambre, X. Dutoit, and B. Schrauwen, in *The 2010 International Joint Conference on Neural Networks (IJCNN)* (IEEE, 2010) p. 1–8.
[28] M. Inubushi and K. Yoshimura, Scientific Reports **7**, 10.1038/s41598-017-10257-6 (2017).
[29] E. P. Wigner, in *Philosophical reflections and syntheses* (Springer, 1995) pp. 247–260.
[30] K. Kobayashi, K. Fujii, and N. Yamamoto, PRX Quantum **5**, 040325 (2024).
[31] In the context of the NISQRC algorithm of Ref. [17], these are referred to as the Memory (M) and Readout (R) subsystems.
[32] G. Adesso, D. Girolami, and A. Serafini, Phys. Rev. Lett. **109**, 190502 (2012).
[33] A. Hamma, S. M. Giampaolo, and F. Illuminati, Phys. Rev. A **93**, 012303 (2016).
[34] Nature **622**, 481 (2023).
[35] R. Kukulski, I. Nechita, Ł. Pawela, Z. Puchała, and K. Życzkowski, J. Math. Phys. **62** (2021).
[36] M. Serbyn, D. A. Abanin, and Z. Papić, Nat. Phys. **17**, 675 (2021).
[37] N. Hunter-Jones, arXiv:1905.12053 (2019).
[38] M. M. Wilde, *Quantum information theory* (Cambridge university press, 2013).
[39] W.-K. Mok, T. Haug, A. L. Shaw, M. Endres, and J. Preskill, arXiv:2410.05181 (2024).
[40] R. Belyansky, P. Bienias, Y. A. Kharkov, A. V. Gorshkov, and B. Swingle, Phys. Rev. Lett. **125**, 130601 (2020).
[41] A. Javadi-Abhari, M. Treinish, K. Krsulich, C. J. Wood, J. Lishman, J. Gacon, S. Martiel, P. D. Nation, L. S. Bishop, A. W. Cross, B. R. Johnson, and J. M. Gambetta, Quantum computing with Qiskit (2024), arXiv:2405.08810 [quant-ph].
[42] A. Elben, B. Vermersch, C. F. Roos, and P. Zoller, Phys.

Rev. A **99**, 052323 (2019).
[43] Y. Li, Y. Zou, P. Glorioso, E. Altman, and M. P. Fisher, Phys. Rev. Lett. **130**, 220404 (2023).
[44] A. Elben, S. T. Flammia, H.-Y. Huang, R. Kueng, J. Preskill, B. Vermersch, and P. Zoller, Nat. Rev. Phys. **5**, 9 (2023).
[45] M. Ippoliti and W. W. Ho, Quantum **6**, 886 (2022).
[46] S.-X. Zhang, J. Allcock, Z.-Q. Wan, S. Liu, J. Sun, H. Yu, X.-H. Yang, J. Qiu, Z. Ye, Y.-Q. Chen, *et al.*, Quantum **7**, 912 (2023).

Appendix A: Equivalence of with/without reset in measurement-conditioned QMI

In this section, we prove that the dynamics of measurement-conditioned QMI remains the same regardless of reset or not. Similar to Eq. (1), the conditional state at step t without reset strategy is

$$|\psi'_{\mathbf{z}}(\boldsymbol{U})\rangle_{RA_t} \tag{A1}$$
$$\propto {}_{\boldsymbol{B}}\langle \boldsymbol{z}| U_t \cdots U_2 U_1 \left[|\Phi\rangle_{RA_0} \otimes \left(|0\rangle_{B_0} \otimes_{k=1}^{t-1} |z_k\rangle_{B_k}\right)\right] \tag{A2}$$
$$\propto {}_{\boldsymbol{B}}\langle \boldsymbol{z}| U_t \cdots U_2 U_1 \left[|\Phi\rangle_{RA_0} \otimes \left(\otimes_{k=1}^{t-1} X^{z_k} |\boldsymbol{0}\rangle_{\boldsymbol{B}}\right)\right] \tag{A3}$$
$$= |\psi_{\mathbf{z}}(\boldsymbol{U}^{\mathbf{z}})\rangle_{RA_t}\,, \tag{A4}$$

where $\boldsymbol{B} = B_t \cdots B_2 B_1$ is the joint system of bath system in each step and we have defined $\boldsymbol{U}^{\mathbf{z}} = U_t X^{z_{t-1}} U_3 X^{z_2} U_2 X^{z_1} U_1$ with $\{X^{z_k}\}_{k=1}^{t-1}$ applied on the bath system only.

Then from the definition of measurement-conditioned QMI in Eq. (4),

$$\mathbb{E}_{\text{Haar}}\, \overline{I(R:A_t|\mathbf{z})}' \tag{A5}$$
$$= \mathbb{E}_{\boldsymbol{U}\sim\text{Haar}}\, 2\,\mathbb{E}_{\mathbf{z}}\, S\left(\text{tr}_R\left(|\psi'_{\mathbf{z}}(\boldsymbol{U})\rangle\langle\psi'_{\mathbf{z}}(\boldsymbol{U})|_{RA_t}\right)\right) \tag{A6}$$
$$= 2\,\mathbb{E}_{\boldsymbol{U}\sim\text{Haar}} \sum_{\boldsymbol{z}} P_{\boldsymbol{U}^{\boldsymbol{z}}}(\boldsymbol{z}) S\left(\text{tr}_R\left(|\psi_{\mathbf{z}}(\boldsymbol{U}^{\mathbf{z}})\rangle\langle\psi_{\mathbf{z}}(\boldsymbol{U}^{\mathbf{z}})|_{RA_t}\right)\right) \tag{A7}$$
$$= 2\sum_{\boldsymbol{z}} \mathbb{E}_{\boldsymbol{U}\sim\text{Haar}}\, P_{\boldsymbol{U}^{\boldsymbol{z}}}(\boldsymbol{z}) S\left(\text{tr}_R\left(|\psi_{\mathbf{z}}(\boldsymbol{U}^{\mathbf{z}})\rangle\langle\psi_{\mathbf{z}}(\boldsymbol{U}^{\mathbf{z}})|_{RA_t}\right)\right) \tag{A8}$$
$$= \mathbb{E}_{\text{Haar}}\, \overline{I(R:A_t|\mathbf{z})} \tag{A9}$$

equals the original measurement-conditioned QMI with reset strategy.

Appendix B: Identical unitary or random unitary

In this section, we provide additional numerical simulations to compare the QMI dynamics and its corresponding lifetime in quantum dynamics with randomly-sampled unitary and identical unitaries. To be precise, in the main text, for Haar quantum dynamics, we randomly sample t unitaries $\{U_k\}_{k=1}^t$ from Haar ensemble. Therefore, we regard this as random Haar dynamics; meanwhile for Hamiltonian-based quantum dynamics, we randomly choose a group of parameters $\{\eta_i^x, \eta_i^z, J_{ij}\}$ and keep it fixed for all $\{U_k\}_{k=1}^t$, which we regard as identical Hamiltonian dynamics. We also consider two additional cases here. For identical Haar quantum dynamics, we randomly sample a single unitary U from Haar ensemble and utilize it across the dynamics for t steps; for random Hamiltonian-based quantum dynamics, we randomly choose t groups of parameters for the Hamiltonian in Eq. (7), and take their evolution for unitaries in each step.

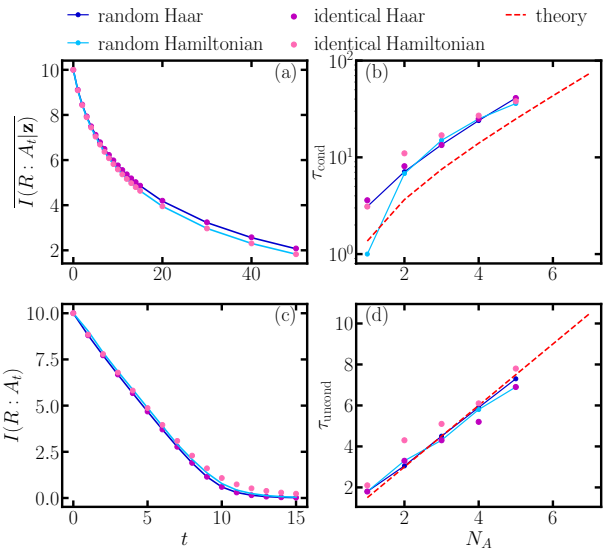

Figure 11. Comparisons on dynamics of QMI and the corresponding lifetime in quantum dynamics with random unitary and identical unitary. We present measurement-conditioned QMI and measurement-unconditioned QMI in top and bottom panels. Dark and light blue lines represent numerical simulations with randomly sampled Haar unitary and random Hamiltonian evolution separately. Purple and pink dots show results with identical fixed Haar unitary and fixed Hamiltonian evolution separately. Red dashed line in (b) and (d) represent theory from Eq. (10) and Eq. (18) with $\epsilon = 1/4$. In (a) and (c), we have system of $N_A = 5$ data qubits. In all cases, the bath consists of $N_B = 1$ qubits.

In Fig. 11, we numerically simulate the measurement-conditioned and unconditioned QMI dynamics for the four cases above and estimate the corresponding QMI lifetime. The QMI dynamics for identical Haar and Hamiltonian evolution (purple and pink) overlap with the results for random Haar and Hamiltonian (dark and light blue) for a system of $N_A = 5$ data qubits. The QMI lifetime among the four cases also approach each other in the same asymptotic scaling though with deviations at small N_A. To conclude, given a large system size of N_A, the QMI dynamics with random unitaries or identical unitaries become indistinguishable, making our theories of Theorem 1 and Theorem 2 applicable to wide scenarios of quantum dynamics from holographic thermalization to reservoir computing.

Appendix C: Residual monitored dynamics

In this section, we provide numerical evidence on the decay of QMI in time beyond the lifetime $\tau_{\rm cond}$ in Eq. (10). As the lower bound Eq. (8) (or the simplified version Eq. (9)) becomes negative at extremely late time, we expect deviations from the lower bound. For the quantum states under consideration though, these residual dynamics correspond to $t \gg \tau_{\rm cond}$, which is beyond exponential in system size. Moreover, at this point the QMI is already infinitesimal and less interesting. Nevertheless, we present some numerical results demonstrating the exponential decay for $t \gg \tau_{\rm cond}$ in Fig. 12a. Here we choose the initial state for different N_A to be the conditional state in Eq. (1) with Bell state $|\Phi\rangle$ and $\mathbf{z} = (\mathbf{0}, \cdots \mathbf{0})$ at $t \gg \tau_{\rm cond}$. The exponential decay of QMI further indicates that the logarithmic decay of QMI identified in Theorem 1 is *not* universal for *all* states, despite proven for Bell state and generic for various states considered above. Counterexample can be constructed by initializing the quantum state in the state at $t \gg \tau_{\rm cond}$ in those cases, as demonstrated by the exponential decay starting from time zero in our numerical examples. Despite the exponential decay with time, we find that the lifetime versus the system size N_A is still exponential, as shown in Fig. 12b (blue dots). This is because the exponent v in the exponential decay $\overline{I(R:A_t|\mathbf{z})} \sim e^{-vt}$ is vanishing as the system size increases (red dots). Furthermore, we would like to point out that our conclusion on the equivalence between cases with and without reset in measurement-conditioned QMI still holds, as shown via the comparison in Fig. 12c.

Appendix D: Derivation for measurement-conditioned QMI (Theorem 1)

In this section, we derive the dynamics of measurement-conditioned QMI. We begin with the lower bound to connect the measurement-conditioned QMI to purity of reduced state.

$$\begin{aligned}
\overline{I(R:A_t|\mathbf{z})} &\equiv \mathbb{E}_{\mathbf{z}}\left[S(R|\mathbf{z}) + S(A_t|\mathbf{z}) - S(RA_t|\mathbf{z})\right] && \text{(D1)}\\
&= \mathbb{E}_{\rm Haar}\,\mathbb{E}_{\mathbf{z}}\, 2S(A_t|\mathbf{z}) && \text{(D2)}\\
&\geq \mathbb{E}_{\mathbf{z}}\, 2S_2(A_t|\mathbf{z}) = -2\,\mathbb{E}_{\mathbf{z}} \log_2\left(\mathrm{tr}\left(\rho^2_{A_t|\mathbf{z}}\right)\right) && \text{(D3)}\\
&\geq -2\log_2\left(\mathbb{E}_{\mathbf{z}}\,\mathrm{tr}\left(\rho^2_{A_t|\mathbf{z}}\right)\right), && \text{(D4)}
\end{aligned}$$

where $S(A_t|\mathbf{z})$ is the von Neumann entanglement entropy of the reduced state $\rho_{A_t|\mathbf{z}} = \mathrm{tr}_R(|\psi_{\mathbf{z}}\rangle\langle\psi_{\mathbf{z}}|_{RA_t})$ and so as others. The second line comes from the fact that the conditional state $|\psi_{\mathbf{z}}\rangle_{RA_t}$ is a pure state. We utilize the monotonicity in Rényi entropy to obtain Ineq. (D3), and obtain the last inequality utilizing the concavity of logarithmic function. Utilizing the concavity property again, we can obtain the lower bound for the Haar-averaged measurement-conditioned QMI as

$$\mathbb{E}_{\rm Haar}\,\overline{I(R:A_t|\mathbf{z})} \geq -2\log_2\left(\mathbb{E}_{\rm Haar}\,\mathbb{E}_{\mathbf{z}}\,\mathrm{tr}\left(\rho^2_{A_t|\mathbf{z}}\right)\right). \tag{D5}$$

Via the bath equivalent expansion in Fig. 13, we can first write out the linear map E (blue box) as

$$E = \sum_{\boldsymbol{a},\boldsymbol{b}} \prod_{k=0}^{t-1} \langle a_{k+1} b_{2k+1}|U_k|a_k b_{2k}\rangle\, |a_t\rangle_{A_t}\, \langle a_0|_{A_0} \otimes_{k=0}^{t-1} \langle b_{2k+1}|\, \langle b_{2k}|\,, \tag{D6}$$

where $\boldsymbol{a} = (a_0, \cdots, a_t)$ and $\boldsymbol{b} = (b_0, b_1, \cdots, b_{2t-2}, b_{2t-1})$ are vector representations of indices. By applying the linear map E on the maximally entangled state $|\Phi\rangle_{RA_0}$, we have

$$E' \equiv (\mathbb{I}_R \otimes E)\,|\Phi\rangle_{RA_0} = \frac{1}{\sqrt{d_A}} \sum_{\boldsymbol{a},\boldsymbol{b}} \prod_{k=0}^{t-1} \langle a_{k+1} b_{2k+1}|U_k|a_k b_{2k}\rangle\, |a_0\rangle_R\, |a_t\rangle_{A_t} \otimes_{k=0}^{t-1} \langle b_{2k+1}|\, \langle b_{2k}|\,, \tag{D7}$$

which is a linear map from the expanded bath including input and measurement to the output conditional state in system RA_t. The same formalism is also adopted in Ref. [7, 45]. From Fig. 13, the temporal input generated from the green dashed box is $|\phi_{\mathbf{z}}\rangle = \otimes_{k=0}^{t-1} |z_t\rangle\,|0\rangle$, and therefore we can obtain the output conditional state and measurement probability as

$$\begin{cases} |\psi_{\mathbf{z}}\rangle_{RA_t} & = E'\,|\phi_{\mathbf{z}}\rangle\,/\sqrt{P(\mathbf{z})} \\ P(\mathbf{z}) & = \langle\phi_{\mathbf{z}}|E'^{\dagger}E'|\phi_{\mathbf{z}}\rangle\,. \end{cases} \tag{D8}$$

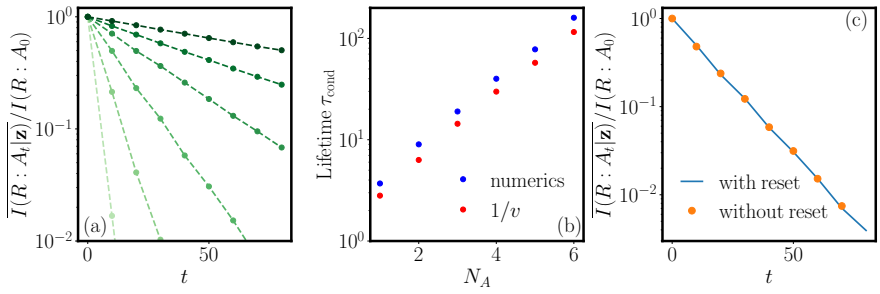

Figure 12. Measurement-conditioned QMI $\overline{I(R:A_t|\mathbf{z})}$ in monitored residual dynamics. The initial state $|\psi\rangle_{RA_0}$ is chosen to be the late-time conditional state in dynamics with Bell initial state. In (a), we plot the normalized QMI dynamics for $N_A = 1$ to 6 (light to dark). In (b), blue dots correspond to the estimated lifetime from numerical simulation in (a) for $\epsilon = 1/4$ and red dots represent the scaling of $1/v$ where v is the rate from linear fitting of $\overline{I(R:A_t|\mathbf{z})} \sim e^{-vt}$. In (c), we compare the numerical simulation of QMI dynamics with (blue) and without reset (orange) in a system of $N_A = 3$ qubits. In all cases, we take $N_B = 1$ bath qubits.

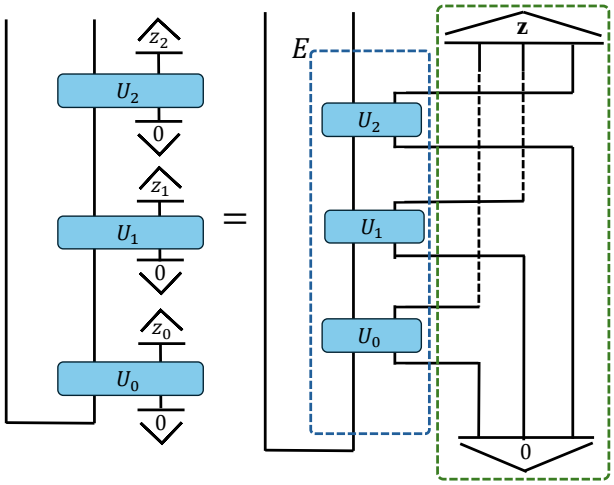

Figure 13. Equivalent relation on the quantum dynamics with mid-circuit measurements and zero state reset via expanding the bath. The linear map E (blue box) is applied on the initial maximally entangled state. The dashed lines indicate that those outputs are directly connected to the measurement results $|\boldsymbol{z}\rangle$. Blue box shows the linear map E, green dashed box shows the temporal input $|\phi_{\mathbf{z}}\rangle$. Here we show an example for $t = 3$.

The corresponding density operator is $|\psi_{\mathbf{z}}\rangle\langle\psi_{\mathbf{z}}|_{RA_t} = P(\mathbf{z})^{-1} E' |\phi_{\mathbf{z}}\rangle\langle\phi_{\mathbf{z}}| E'^{\dagger}$, and the reduced state $\rho_{A_t|\mathbf{z}}$ is

$$\rho_{A_t|\mathbf{z}} = P(\mathbf{z})^{-1} \operatorname{tr}_R(E' |\phi_{\mathbf{z}}\rangle\langle\phi_{\mathbf{z}}| E'^{\dagger}). \tag{D9}$$

The measured-conditioned purity of $\rho_{A_t|\mathbf{z}}$ is thus

$$\overline{\gamma} \equiv \mathbb{E}_{\mathbf{z}} \operatorname{tr}\left(\rho^2_{A_t|bfz}\right) = \sum_{\mathbf{z}} P(\mathbf{z}) \operatorname{tr}\left(\rho^2_{A_t|\mathbf{z}}\right) \tag{D10}$$

$$= \sum_{\mathbf{z}} P(\mathbf{z}) P(\mathbf{z})^{-2} \operatorname{tr}\left(\operatorname{tr}_R(E' |\phi_{\mathbf{z}}\rangle\langle\phi_{\mathbf{z}}| E'^{\dagger})^2\right) \tag{D11}$$

$$= \sum_{\mathbf{z}} P(\mathbf{z})^{-1} \operatorname{tr}\left(E'^{\otimes 2} |\phi_{\mathbf{z}}\rangle\langle\phi_{\mathbf{z}}|^{\otimes 2} E'^{\dagger\otimes 2} (\mathbb{I}_R \otimes \mathbb{S}_{A_t})\right) \tag{D12}$$

$$= \sum_{\mathbf{z}} \langle\phi_{\mathbf{z}}|E'^{\dagger}E'|\phi_{\mathbf{z}}\rangle^{-1} \operatorname{tr}\left(E'^{\otimes 2} |\phi_{\mathbf{z}}\rangle\langle\phi_{\mathbf{z}}|^{\otimes 2} E'^{\dagger\otimes 2} (\mathbb{I}_R \otimes \mathbb{S}_{A_t})\right), \tag{D13}$$

where $\mathbb{S}_{A_t}$ is the swap operator over two replicas in system A_t. To evaluate it analytically, we introduce the pseudo

measurement-conditioned purity from replica trick as

$$\overline{\gamma}^{(m)} = \sum_{\mathbf{z}} \langle\phi_{\mathbf{z}}|E'^{\dagger}E'|\phi_{\mathbf{z}}\rangle^m \operatorname{tr}\Big(E'^{\otimes 2}\left|\phi_{\mathbf{z}}\right\rangle\!\left\langle\phi_{\mathbf{z}}\right|^{\otimes 2} E'^{\dagger\otimes 2}(\mathbb{I}_R\otimes\mathbb{S}_{A_t})\Big) \tag{D14}$$

$$= \sum_{\mathbf{z}} \operatorname{tr}\big(E'\left|\phi_{\mathbf{z}}\right\rangle\!\left\langle\phi_{\mathbf{z}}\right| E'^{\dagger}\big)^m \operatorname{tr}\Big(E'^{\otimes 2}\left|\phi_{\mathbf{z}}\right\rangle\!\left\langle\phi_{\mathbf{z}}\right|^{\otimes 2} E'^{\dagger\otimes 2}(\mathbb{I}_R\otimes\mathbb{S}_{A_t})\Big) \tag{D15}$$

$$= \sum_{\mathbf{z}} \operatorname{tr}\Big(E'^{\otimes m}\left|\phi_{\mathbf{z}}\right\rangle\!\left\langle\phi_{\mathbf{z}}\right|^{\otimes m} E'^{\dagger\otimes m}\Big) \operatorname{tr}\Big(E'^{\otimes 2}\left|\phi_{\mathbf{z}}\right\rangle\!\left\langle\phi_{\mathbf{z}}\right|^{\otimes 2} E'^{\dagger\otimes 2}(\mathbb{I}_R\otimes\mathbb{S}_{A_t})\Big) \tag{D16}$$

$$= \sum_{\mathbf{z}} \operatorname{tr}\Big(E'^{\otimes(m+2)}\left|\phi_{\mathbf{z}}\right\rangle\!\left\langle\phi_{\mathbf{z}}\right|^{\otimes(m+2)} E'^{\dagger\otimes(m+2)}(\mathbb{I}_R\otimes(\mathbb{I}_m\otimes\mathbb{S}_{A_t}))\Big) \tag{D17}$$

$$= \operatorname{tr}\left(E'^{\otimes(m+2)}\left(\sum_{\mathbf{z}}\left|\phi_{\mathbf{z}}\right\rangle\!\left\langle\phi_{\mathbf{z}}\right|^{\otimes(m+2)}\right) E'^{\dagger\otimes(m+2)}(\mathbb{I}_R\otimes(\mathbb{I}_m\otimes\mathbb{S}_{A_t}))\right), \tag{D18}$$

where in the last step $\mathbb{I}_R$ is changed to the identity operator on $m+2$ replicas and $\mathbb{I}_m\otimes\mathbb{S}_{A_t}$ is the swap operator on A_t with trivial identity on first m replicas. Note that

$$\sum_{\mathbf{z}}\left|\phi_{\mathbf{z}}\right\rangle\!\left\langle\phi_{\mathbf{z}}\right|^{\otimes(m+2)} = \sum_{\mathbf{z}} \otimes_{k=0}^{t-1}\left|z_k\right\rangle\!\left\langle z_k\right|^{\otimes(m+2)}\otimes\left|0\right\rangle\!\left\langle 0\right|^{\otimes(m+2)} \tag{D19}$$

$$= \otimes_{k=0}^{t-1}\left(\sum_{z_k}\left|z_k\right\rangle\!\left\langle z_k\right|^{\otimes(m+2)}\otimes\left|0\right\rangle\!\left\langle 0\right|^{\otimes(m+2)}\right) \tag{D20}$$

$$\equiv \otimes_{k=0}^{t-1}\left(D_{m+2}\otimes\left|0\right\rangle\!\left\langle 0\right|^{\otimes(m+2)}\right), \tag{D21}$$

where we define $D_{m+2}=\sum_z\left|z\right\rangle\!\left\langle z\right|^{\otimes(m+2)}$. Then we can evaluate $E^{\otimes(m+2)}\left(\sum_{\mathbf{z}}\left|\phi_{\mathbf{z}}\right\rangle\!\left\langle\phi_{\mathbf{z}}\right|^{\otimes(m+2)}\right)E^{\dagger\otimes(m+2)}$ as

$$\begin{aligned}
&E'^{\otimes(m+2)}\left(\sum_{\mathbf{z}}\left|\phi_{\mathbf{z}}\right\rangle\!\left\langle\phi_{\mathbf{z}}\right|^{\otimes(m+2)}\right)E'^{\dagger\otimes(m+2)}\\
&= d_A^{-(m+2)}\sum_{\substack{\boldsymbol{\alpha},\boldsymbol{\beta},\\ \boldsymbol{\alpha}',\boldsymbol{\beta}'}}\prod_{k=0}^{t-1}\langle\alpha_{k+1}\beta_{2k+1}|U_k^{\otimes(m+2)}|\alpha_k\beta_{2k}\rangle\,\langle\alpha'_k\beta'_{2k}|U_k^{\dagger\otimes(m+2)}|\alpha'_{k+1}\beta'_{2k+1}\rangle\,\left|\alpha_0\right\rangle\!\left\langle\alpha'_0\right|_R\left|\alpha_t\right\rangle\!\left\langle\alpha'_t\right|_{A_t}\\
&\qquad\times\otimes_{k=0}^{t-1}\langle\beta_{2k+1}|D_{m+2}|\beta'_{2k+1}\rangle\,\langle\beta_{2k}|0^{m+2}\rangle\,\langle 0^{m+2}|\beta'_{2k}\rangle\,,
\end{aligned}\tag{D22}$$

where $|\alpha_k\rangle=\otimes_{j=1}^{m+2}|a_k^{(j)}\rangle\,,|\beta_k\rangle=\otimes_{j=1}^{m+2}|b_k^{(j)}\rangle\,,|\alpha'_k\rangle=\otimes_{j=1}^{m+2}|a_k'^{(j)}\rangle\,,|\beta'_k\rangle=\otimes_{j=1}^{m+2}|b_k'^{(j)}\rangle$ are the simplified notation for $m+2$ replicas of basis. $\boldsymbol{\alpha}=(\alpha_0,\cdots,\alpha_{t-1})$, $\boldsymbol{\beta}=(\beta_0,\beta_1,\cdots,\beta_{2k-2},\beta_{2k-1})$ are the vector representations and so as the others $\boldsymbol{\alpha}',\boldsymbol{\beta}'$. Utilizing the facts

$$\langle\beta_{2k+1}|D_{m+2}|\beta'_{2k+1}\rangle=\sum_{z_k}\langle\beta_{2k+1}|z_k^{\otimes(m+2)}\rangle\,\langle z_k^{\otimes(m+2)}|\beta'_{2k+1}\rangle=\sum_{z_k}\delta_{\beta_{2k+1},z_k}\delta_{\beta'_{2k+1},z_k}, \tag{D23}$$

$$\langle\beta_{2k}|0^{m+2}\rangle\,\langle 0^{m+2}|\beta'_{2k}\rangle=\delta_{\beta_{2k},0}\delta_{\beta'_{2k},0}, \tag{D24}$$

where $\delta_{\beta,z}=\prod_{j=1}^{m+2}\delta_{b^{(j)},z}$ is a simplified notation of Kronecker deltas on each replicas. Then we have

$$\begin{aligned}
&E'^{\otimes(m+2)}\left(\sum_{\mathbf{z}}\left|\phi_{\mathbf{z}}\right\rangle\!\left\langle\phi_{\mathbf{z}}\right|^{\otimes(m+2)}\right)E'^{\dagger\otimes(m+2)}\\
&= d_A^{-(m+2)}\sum_{\boldsymbol{\alpha},\boldsymbol{\alpha}'}\sum_{\mathbf{z}}\prod_{k=0}^{t-1}\langle\alpha_{k+1}z_k^{\otimes(m+2)}|U_k^{\otimes(m+2)}|\alpha_k 0^{\otimes(m+2)}\rangle\,\langle\alpha'_k 0^{\otimes(m+2)}|U_k^{\dagger\otimes(m+2)}|\alpha'_{k+1}z_k^{\otimes(m+2)}\rangle\,\left|\alpha_0\right\rangle\!\left\langle\alpha'_0\right|_R\left|\alpha_t\right\rangle\!\left\langle\alpha'_t\right|_{A_t}
\end{aligned}\tag{D25}$$

$$= d_A^{-(m+2)}\sum_{\boldsymbol{\alpha},\boldsymbol{\alpha}'}\sum_{\mathbf{z}}\prod_{k=0}^{t-1}\operatorname{tr}\left(U_k^{\otimes(m+2)}\left(\left|\alpha_k\right\rangle\!\left\langle\alpha'_k\right|\otimes\left|0\right\rangle\!\left\langle 0\right|^{\otimes(m+2)}\right)U_k^{\dagger\otimes(m+2)}\left(\left|\alpha'_{k+1}\right\rangle\!\left\langle\alpha_{k+1}\right|\otimes\left|z_k\right\rangle\!\left\langle z_k\right|^{\otimes(m+2)}\right)\right)\left|\alpha_0\right\rangle\!\left\langle\alpha'_0\right|_R\left|\alpha_t\right\rangle\!\left\langle\alpha'_t\right|_{A_t}. \tag{D26}$$

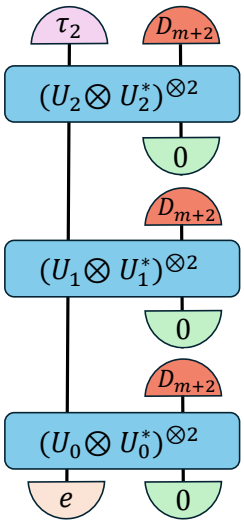

Figure 14. Tensor network representation of Haar-averaged pseudo measurement-conditioned purity of $\rho_{A_t|\mathbf{z}}$ with time steps $t = 3$. Here $\tau_2 = \mathbb{I}_m \otimes \mathbb{S}$ is the swap operator on the last two replicas.

The pseudo measurement-conditioned purity (Eq. (D18)) then becomes

$$\overline{\gamma}^{(m)} = \mathrm{tr}\left(E'^{\otimes(m+2)}\left(\sum_{\mathbf{z}} |\phi_{\mathbf{z}}\rangle\langle\phi_{\mathbf{z}}|^{\otimes(m+2)}\right) E'^{\dagger\otimes(m+2)}(\mathbb{I}_R \otimes (\mathbb{I}_m \otimes \mathbb{S}_{A_t}))\right) \tag{D27}$$

$$= d_A^{-(m+2)} \sum_{\boldsymbol{\alpha},\boldsymbol{\alpha}'} \sum_{\mathbf{z}} \prod_{k=0}^{t-1} \mathrm{tr}\left(U_k^{\otimes(m+2)}\left(|\alpha_k\rangle\langle\alpha'_k| \otimes |0\rangle\langle 0|^{\otimes(m+2)}\right) U_k^{\dagger\otimes(m+2)}\left(\left|\alpha'_{k+1}\right\rangle\left\langle\alpha_{k+1}\right| \otimes |z_k\rangle\langle z_k|^{\otimes(m+2)}\right)\right)$$
$$\times \langle\alpha'_0|\alpha_0\rangle_R \langle\alpha'_t|\mathbb{I}_m \otimes \mathbb{S}_{A_t}|\alpha_t\rangle_{A_t} \tag{D28}$$

$$= d_A^{-(m+2)} \sum_{\boldsymbol{\alpha},\boldsymbol{\alpha}'} \prod_{k=0}^{t-1} \mathrm{tr}\left(U_k^{\otimes(m+2)}\left(|\alpha_k\rangle\langle\alpha'_k| \otimes |0\rangle\langle 0|^{\otimes(m+2)}\right) U_k^{\dagger\otimes(m+2)}\left(\left|\alpha'_{k+1}\right\rangle\left\langle\alpha_{k+1}\right| \otimes D_{m+2}\right)\right)$$
$$\times \prod_{j=1}^{m+2} \delta_{a_0^{(j)},a_0'^{(j)}} \prod_{j=1}^{m} \delta_{a_t^{(j)},a_t'^{(j)}} \delta_{a_t'^{(m+1)},a_t^{(m+2)}} \delta_{a_t'^{(m+2)},a_t^{(m+1)}}. \tag{D29}$$

Next, we evaluate Haar ensemble average on the pseudo measurement-conditioned purity $\overline{\gamma}^{(m)}$. For Haar unitary twirling, it is known that

$$\mathbb{E}_{\mathrm{Haar}}\left[U^{\otimes(m+2)} \otimes U^{*\otimes(m+2)}\right] = \sum_{\sigma,\pi\in S_{m+2}} \mathrm{Wg}(\sigma^{-1}\pi, m+2)|\hat{\sigma})(\hat{\pi}| \tag{D30}$$

$$= \mathrm{Wg}(e, m+2)\sum_{\pi} |\hat{\pi})(\hat{\pi}| + \sum_{\sigma\neq\pi} \mathrm{Wg}(\sigma^{-1}\pi, m+2)|\hat{\sigma})(\hat{\pi}|, \tag{D31}$$

where S_{m+2} is the permutation group of $m+2$ replicas, and $\hat{\pi}$ is the operator representation of permutation π. $\mathrm{Wg}(\sigma^{-1}\pi, m+2) = (d^{|\sigma^{-1}\pi|})^{-1}$ is the Weingarten coefficient with $|\sigma^{-1}\pi|$ to be the number of cycles of permutation $\sigma^{-1}\pi$.

We start from the unitary twirling on the last step boundary condition,

$$\mathbb{E}_{\mathrm{Haar}}\left[U_{t-1}^{\otimes(m+2)} \otimes U_{t-1}^{*\otimes(m+2)}\right] |\tau_2)_A |D_{m+2})_B$$
$$= \mathrm{Wg}(e, m+2)\sum_{\pi} |\hat{\pi})_{AB}(\hat{\pi}|\tau_2)_A(\hat{\pi}|D_{m+2})_B + \sum_{\sigma\neq\pi} \mathrm{Wg}(\sigma^{-1}\pi, m+2)|\hat{\sigma})_{AB}(\hat{\pi}|\tau_2)_A(\hat{\pi}|D_{m+2})_B. \tag{D32}$$

In the following, we evaluate the two terms above separately. For the first term, note that $(\hat{\pi}|D_{m+2})_B =$

$\mathrm{tr}\left(\hat{\pi}^\dagger \sum_z |z\rangle\langle z|^{\otimes(m+2)}\right) = \sum_z \langle z^{\otimes(m+2)}|\hat{\pi}^\dagger|z^{\otimes(m+2)}\rangle = d_B$, we then have

$$\mathrm{Wg}(e, m+2) \sum_\pi |\hat{\pi})_{AB}(\hat{\pi}|\tau_2)_A(\hat{\pi}|D_{m+2})_B = \mathrm{Wg}(e, m+2) d_B \sum_\pi d_A^{|\pi^\dagger \tau_2|}|\hat{\pi})_{AB}, \tag{D33}$$

and further connecting $|D_{m+2})(0|_B$ on the bath system, we have

$$\begin{aligned}
&|D_{m+2})(0|_B \mathrm{Wg}(e, m+2) \sum_\pi |\hat{\pi})_{AB}(\hat{\pi}|\tau_2)_A(\hat{\pi}|D_{m+2})_B \\
&= \mathrm{Wg}(e, m+2) d_B \sum_\pi d_A^{|\pi^\dagger \tau_2|}|\hat{\pi})_A |D_{m+2})_B \qquad \text{(D34)} \\
&\simeq \mathrm{Wg}(e, m+2) d_B \left(d_A^{m+2}|\tau_2)_A + d_A^{m+1}|e)_A\right)|D_{m+2})_B, \qquad \text{(D35)}
\end{aligned}$$

where we keep the leading order terms $\pi = \tau_2, \mathbb{I}$ in the last step give large system size $d_A \gg 1$. Similarly, for the second term in Eq. (D32), we have

$$\begin{aligned}
&|D_{m+2})(0|_B \sum_{\sigma\neq\pi} \mathrm{Wg}(\sigma^{-1}\pi, m+2)|\hat{\sigma})_{AB}(\hat{\pi}|\tau_2)_A(\hat{\pi}|D_{m+2})_B \\
&\simeq d_B \left[\mathrm{Wg}(e\tau_2, m+2) d_A^{m+2}|e)_A|D_{m+2})_B + \mathrm{Wg}(\tau_2^{-1}e, m+2) d_A^{m+1}|\tau_2)_A|D_{m+2})_B\right] \qquad \text{(D36)} \\
&= \mathrm{Wg}(e\tau_2, m+2) d_A^{m+1} d_B \left(d_A|e)_A + |\tau_2)_A\right)|D_{m+2})_B, \qquad \text{(D37)}
\end{aligned}$$

where in the second line we still focus on the leading order $(\sigma, \pi) = (\tau_2, e), (e, \tau_2)$. Combining these two terms together, we have

$$\begin{aligned}
&|D_{m+2})(0|_B \mathbb{E}_{\mathrm{Haar}}\left[U_{t-1}^{\otimes(m+2)} \otimes {U_{t-1}^*}^{\otimes(m+2)}\right]|\tau_2)_A|D_{m+2})_B \\
&\simeq \mathrm{Wg}(e, m+2) d_A^{m+1} d_B \left(d_A|\tau_2)_A + |e)_A\right)|D_{m+2})_B + \mathrm{Wg}(e\tau_2, m+2) d_A^{m+1} d_B \left(d_A|e)_A + |\tau_2)_A\right)|D_{m+2})_B \qquad \text{(D38)} \\
&\simeq \frac{d_A^{m+1} d_B}{d_A^{m+2} d_B^{m+2}} \left(d_A|\tau_2)_A + |e)_A\right)|D_{m+2})_B - \frac{d_A^{m+1} d_B}{d_A^{m+3} d_B^{m+3}} \left(d_A|e)_A + |\tau_2)_A\right)|D_{m+2})_B \qquad \text{(D39)} \\
&= d_B^{-(m+1)}\left(1 - d_A^{-2} d_B^{-1}\right)|\tau_2)_A|D_{m+2})_B + d_A^{-1} d_B^{-(m+1)}\left(1 - d_B^{-1}\right)|e)_A|D_{m+2})_B, \qquad \text{(D40)}
\end{aligned}$$

where in the third line we approximate it by $\mathrm{Wg}(e, m+2) \simeq d_A^{-(m+2)} d_B^{-(m+2)}$ and $\mathrm{Wg}(e\tau_2, m+2) \simeq -d_A^{-(m+3)} d_B^{-(m+3)}$ given $d_A \gg 1$. Let's move to the next twirling of U_{t-2} and bath operation $|D_{m+2})(0|_B$. For the boundary condition $|e)_A|D_{m+2})_B$, we have

$$\begin{aligned}
&|D_{m+2})(0|_B \mathbb{E}_{\mathrm{Haar}}\left[U_{t-2}^{\otimes(m+2)} \otimes {U_{t-2}^*}^{\otimes(m+2)}\right]|e)_A|D_{m+2})_B \\
&= |D_{m+2})(0|_B \sum_{\sigma,\pi} \mathrm{Wg}(\sigma^{-1}\pi, m+2)|\hat{\sigma})_{AB}(\hat{\pi}|e)_A(\hat{\pi}|D_{m+2})_B \qquad \text{(D41)} \\
&= d_B \sum_{\sigma,\pi} \mathrm{Wg}(\sigma^{-1}\pi, m+2) d_A^{|\pi^\dagger|}|\hat{\sigma})_A|D_{m+2})_B \qquad \text{(D42)} \\
&= d_B \left[\mathrm{Wg}(e, m+2) \sum_\pi d_A^{|\pi^\dagger|}|\hat{\pi})_A + \sum_{\sigma\neq\pi} \mathrm{Wg}(\sigma^{-1}\pi, m+2) d_A^{|\pi^\dagger|}|\hat{\sigma})_A\right]|D_{m+2})_B \qquad \text{(D43)} \\
&\simeq d_B \left[\mathrm{Wg}(e, m+2)\left(d_A^{m+2}|e)_A + d_A^{m+1}|\tau_2)_A\right) + \mathrm{Wg}(\tau_2^{-1}e, m+2) d_A^{m+2}|\tau_2)_A + \mathrm{Wg}(e\tau_2, m+2) d_A^{m+1}|e)_A\right]|D_{m+2})_B \qquad \text{(D44)} \\
&= d_A^{m+1} d_B \left[\left(\mathrm{Wg}(e, m+2) + \mathrm{Wg}(\tau_2^{-1}e, m+2) d_A\right)|\tau_2)_A + \left(\mathrm{Wg}(e, m+2) d_A + \mathrm{Wg}(e\tau_2, m+2)\right)|e)_A\right]|D_{m+2})_B \qquad \text{(D45)} \\
&\simeq d_A^{m+1} d_B \left[\left(d_A^{-(m+2)} d_B^{-(m+2)} - d_A^{-(m+3)} d_B^{-(m+3)} d_A\right)|\tau_2)_A \left(d_A^{-(m+2)} d_B^{-(m+2)} d_A - d_A^{-(m+3)} d_B^{-(m+3)}\right)|e)_A\right]|D_{m+2})_B \qquad \text{(D46)} \\
&= d_A^{-1} d_B^{-(m+1)}\left(1 - d_B^{-1}\right)|\tau_2)_A|D_{m+2})_B + d_B^{-(m+1)}\left(1 - d_A^{-2} d_B^{-1}\right)|e)_A|D_{m+2})_B, \qquad \text{(D47)}
\end{aligned}$$

where we make the same approximations as we utilized above. To summarize, we have the following linear transformation on boundary conditions in every step from Eqs. (E20), (D47)

$$\begin{cases} |\tau_2)_A|D_{n+2})_B \to q_\tau|\tau_2)_A|D_{m+2})_B + q_e|e)_A|D_{m+2})_B \\ |e)_A|D_{n+2})_B \to q_e|\tau_2)_A|D_{m+2})_B + q_\tau|e)_A|D_{m+2})_B \end{cases}, \tag{D48}$$

where $q_\tau = d_B^{-(m+1)}\left(1 - d_A^{-2}d_B^{-1}\right)$ and $q_e = d_A^{-1}d_B^{-(m+1)}\left(1 - d_B^{-1}\right)$ are two coefficients. We can thus write the linear transformation in the form of a two-by-two matrix

$$Q = \begin{pmatrix} q_\tau & q_e \\ q_e & q_\tau \end{pmatrix}, \tag{D49}$$

with bases $|\tau_2)_A|D_{m+2})_B \to (1,0)^T, |e)_A|D_{m+2})_B \to (0,1)^T$. Via diagonalization, we can write out Q^t explicitly as

$$Q^t = \frac{1}{2}\begin{pmatrix} \nu_+^t + \nu_-^t & \nu_+^t - \nu_-^t \\ \nu_+^t - \nu_-^t & \nu_+^t + \nu_-^t \end{pmatrix}, \tag{D50}$$

where $\nu_\pm = q_\tau \pm q_e$ are eigenvalues of Q. Considering the initial boundary condition at step t in Fig. 14, we obtain the boundary condition at step 0 as

$$Q^t(1,0)^T \to \frac{1}{2}\left[(q_\tau + q_e)^t + (q_\tau - q_e)^t\right]|\tau_2)_A|D_{m+2})_B + \frac{1}{2}\left[(q_\tau + q_e)^t - (q_\tau - q_e)^t\right]|e)_A|D_{m+2})_B, \tag{D51}$$

and thus we have the dynamical solution for pseudo measurement-conditioned purity

$$\mathbb{E}_{\text{Haar}}\,\overline{\gamma}^{(m)} \simeq d_A^{-(m+2)}(e|_A(0|_B\left(\frac{1}{2}\left[(q_\tau + q_e)^t + (q_\tau - q_e)^t\right]|\tau_2)_A|D_{m+2})_B + \frac{1}{2}\left[(q_\tau + q_e)^t - (q_\tau - q_e)^t\right]|e)_A|D_{m+2})_B\right) \tag{D52}$$

$$= \frac{1}{2}d_A^{-(m+2)}\left(\left[(q_\tau + q_e)^t + (q_\tau - q_e)^t\right]d_A^{m+1} + \left[(q_\tau + q_e)^t - (q_\tau - q_e)^t\right]d_A^{m+2}\right) \tag{D53}$$

$$= \frac{1}{2d_A}\left[(1+d_A)(q_\tau + q_e)^t + (1-d_A)(q_\tau - q_e)^t\right] \tag{D54}$$

$$= \frac{1}{2d_A}\left[(1+d_A)\left(d_A^{-2}d_B^{-(m+2)}(d_A+1)(d_Ad_B-1)\right)^t + (1-d_A)\left(d_A^{-2}d_B^{-(m+2)}(d_A-1)(d_Ad_B+1)\right)^t\right] \tag{D55}$$

$$= \frac{1}{2d_A}d_A^{-2t}d_B^{-(m+2)t}\left[(d_A+1)^{t+1}(d_Ad_B-1)^t - (d_A-1)^{t+1}(d_Ad_B+1)^t\right], \tag{D56}$$

where we utilize the definition of q_τ, q_e defined above in the second to last line. Via taking the limit $m \to -1$, we solve the Haar-averaged dynamical solution for the measurement-conditioned purity of $\rho_{A_t|\mathbf{z}}$ as

$$\mathbb{E}_{\text{Haar}}\,\mathbb{E}_{\mathbf{z}}\,\text{tr}\left(\rho_{A_t|\mathbf{z}}^2\right) = \mathbb{E}_{\text{Haar}}\,\overline{\gamma} = \lim_{m\to-1}\mathbb{E}_{\text{Haar}}\,\overline{\gamma}^{(m)} \tag{D57}$$

$$\simeq \frac{1}{2}d_A^{-(2t+1)}d_B^{-t}\left[(d_A+1)^{t+1}(d_Ad_B-1)^t - (d_A-1)^{t+1}(d_Ad_B+1)^t\right]. \tag{D58}$$

Finally, we have the asymptotic lower bound for Haar-averaged measurement-conditioned QMI from Eq. (8)

$$\mathbb{E}_{\text{Haar}}\,\overline{I(R:A_t|\mathbf{z})} \geq -2\log_2\left(\mathbb{E}_{\text{Haar}}\,\mathbb{E}_{\mathbf{z}}\,\text{tr}\left(\rho_{A_t|\mathbf{z}}^2\right)\right) \tag{D59}$$

$$\gtrsim -2\log_2\left(\frac{1}{2}d_A^{-(2t+1)}d_B^{-t}\left[(d_A+1)^{t+1}(d_Ad_B-1)^t - (d_A-1)^{t+1}(d_Ad_B+1)^t\right]\right) \tag{D60}$$

$$= 2 + 2(2t+1)N_A + 2tN_B - 2\log_2\left[(d_A+1)^{t+1}(d_Ad_B-1)^t - (d_A-1)^{t+1}(d_Ad_B+1)^t\right] \tag{D61}$$

$$= 2 + 2(2t+1)N_A + 2tN_B - 2\log_2\left[(d_Ad_B+1)^t(d_A+1)^{t+1}\right] - 2\log_2\left[\left(\frac{d_Ad_B-1}{d_Ad_B+1}\right)^t - \left(\frac{d_A-1}{d_A+1}\right)^{t+1}\right], \tag{D62}$$

which is the solution of Eq. (8) of Theorem. 1 in the main text.

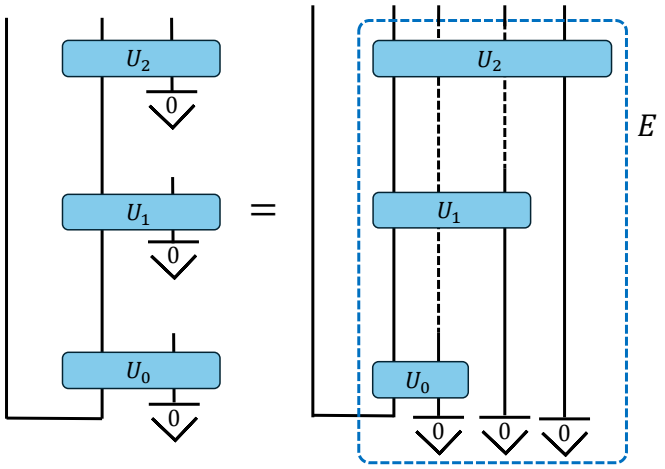

Figure 15. Equivalent relation on the quantum dynamics with mid-circuit measurements and $|0\rangle_B$ reset via expanding the bath. The linear map E (blue box) is applied on the initial maximally entangled state. The dashed lines indicate that those outputs do not interact with the unitaries to be passed through. Here we show an example for $t = 3$.

At the end of this section, we perform an asymptotic analysis on the scaling of above result in the limit of large system size $d_A \gg 1$.

$$\mathbb{E}_{\text{Haar}}\, \overline{I(R:A_t|\mathbf{z})}$$

$$= 2 + 2(2t+1)N_A + 2tN_B - 2t\log_2(d_A d_B + 1) - 2(t+1)\log_2(d_A+1) - 2\log_2\left[\left(1 - \frac{2}{d_A d_B + 1}\right)^t - \left(1 - \frac{2}{d_A+1}\right)^{t+1}\right] \tag{D63}$$

$$\simeq 2 + 2(2t+1)N_A + 2tN_B - 2t(N_A+N_B) - 2(t+1)N_A - 2\log_2\left[1 - \frac{2t}{d_A d_B+1} - \left(1 - \frac{2(t+1)}{d_A+1}\right)\right] \tag{D64}$$

$$= 2 - 2\log_2\left(\frac{2(t+1)}{d_A+1} - \frac{2t}{d_A d_B+1}\right) \tag{D65}$$

$$\simeq 2 - 2\log_2\left(\frac{2(t+1)}{d_A} - \frac{2t}{d_A d_B}\right) \tag{D66}$$

$$= 2 - 2\log_2\left(\frac{2}{d_A}(t+1-t/d_B)\right) \tag{D67}$$

$$= 2N_A - \log_2\left((1-1/d_B)t+1\right). \tag{D68}$$

Appendix E: Derivation for measurement-unconditioned QMI (Theorems 2 and 3)

In this section, we provide the proof on the dynamics for measurement-unconditioned QMI with pure and mixed state reset strategy. As we point out in the main text, for computation convenience, we focus on the Rényi-extended QMI defined by

$$I_2(R:A_t) = S_2(\rho_R) + S_2(\rho_{A_t}) - S_2(\rho_{RA_t}), \tag{E1}$$

where $S_2(\cdot)$ is the Rényi-2 entropy.

In the following, Theorem 2 is proven in Section E 1 and Theorem 3 is proven in Section E 2.

1. Pure-state reset strategy

For pure-state reset strategy, without loosing generality, we simply assume in every step, the bath system is reset to the trivial product state $|0\rangle$. From the equivalence relation in Fig. 15, we can write out the linear map E as

$$E = \sum_{\boldsymbol{a},\boldsymbol{b}} \prod_{k=0}^{t-1} \langle a_{k+1} b_{k+1}|U_k|a_k 0\rangle \, |a_t\rangle_{A_t} \otimes_{k=0}^{t-1} |b_{k+1}\rangle_{B_{k+1}} \langle a_0|_{A_0} \,, \tag{E2}$$

where $\boldsymbol{a} = (a_0, \cdots, a_t)$ and $\boldsymbol{b} = (b_1, \cdots, b_t)$ are vector representation of the corresponding indices on data and bath system. Given the initial maximally-entangled state $|\Phi\rangle_{RA_0} = \frac{1}{\sqrt{d_A}} \sum_j |j\rangle_R |j\rangle_{A_0}$, then we have the output state on $RA_t\boldsymbol{B}$ to be

$$|\psi\rangle_{RA_t\boldsymbol{B}} = (\mathbb{I}_R \otimes E) |\Phi\rangle_{RA_0} \tag{E3}$$

$$= \sum_{\boldsymbol{a},\boldsymbol{b}} \prod_{k=0}^{t-1} \langle a_{k+1} b_{k+1}|U_k|a_k 0\rangle \, |a_t\rangle_{A_t} \otimes_{k=0}^{t-1} |b_{k+1}\rangle_{B_{k+1}} \left(\boldsymbol{I}_R \otimes \langle a_0|_{A_0}\right) |\Phi\rangle_{RA_0} \tag{E4}$$

$$= \frac{1}{\sqrt{d_A}} \sum_{\boldsymbol{a},\boldsymbol{b}} \prod_{k=0}^{t-1} \langle a_{k+1} b_{k+1}|U_k|a_k 0\rangle \, |a_0\rangle_R |a_t\rangle_{A_t} \otimes_{k=0}^{t-1} |b_{k+1}\rangle_{B_{k+1}} \,. \tag{E5}$$

With one more step, we can write out the corresponding density operator of $|\psi\rangle_{RA_t\boldsymbol{B}}$ as

$$\rho_{RA_t\boldsymbol{B}} = \frac{1}{d_A} \sum_{\substack{\boldsymbol{a},\boldsymbol{a}'\\ \boldsymbol{b},\boldsymbol{b}'}} \prod_{k=0}^{t-1} \langle a_{k+1} b_{k+1}|U_k|a_k 0\rangle \, \langle a'_k 0|U_k^\dagger|a'_{k+1} b'_{k+1}\rangle \, |a_0\rangle\langle a'_0|_R \, |a_t\rangle\langle a'_t|_{A_t} \otimes_{k=0}^{t-1} \left|b_{k+1}\right\rangle\!\left\langle b'_{k+1}\right|_{B_{k+1}} . \tag{E6}$$

Recall the definition of Rényi-extended QMI in Eq. (E1), now we evluate the corresponding reduced states and their Rényi-2 entropy. We begin with ρ_R.

$$\rho_R = \mathrm{tr}_{A_t\boldsymbol{B}}(\rho_{RA_t\boldsymbol{B}}) \tag{E7}$$

$$= \frac{1}{d_A} \sum_{\substack{\boldsymbol{a},\boldsymbol{a}'\\ \boldsymbol{b},\boldsymbol{b}'}} \prod_{k=0}^{t-1} \langle a_{k+1} b_{k+1}|U_k|a_k 0\rangle \, \langle a'_k 0|U_k^\dagger|a'_{k+1} b'_{k+1}\rangle \, |a_0\rangle\langle a'_0|_R \, \delta_{a_t,a'_t} \prod_{k=0}^{t-1} \delta_{b_{k+1},b'_{k+1}} \tag{E8}$$

$$= \frac{1}{d_A} \sum_{\substack{\boldsymbol{a},\boldsymbol{a}'\\ \boldsymbol{b},\boldsymbol{b}'}} \prod_{k=0}^{t-1} \mathrm{tr}\left(U_k \left(|a_k\rangle\langle a'_k| \otimes |0\rangle\langle 0|\right) U_k^\dagger \left(\left|a'_{k+1}\right\rangle\!\left\langle a_{k+1}\right| \otimes \left|b'_{k+1}\right\rangle\!\left\langle b_{k+1}\right|\right)\right) |a_0\rangle\langle a'_0|_R \, \delta_{a_t,a'_t} \prod_{k=0}^{t-1} \delta_{b_{k+1},b'_{k+1}}. \tag{E9}$$

The purity of ρ_R then becomes

$$\begin{aligned}
&\mathrm{tr}\left(\rho_R^2\right) \\
&= \frac{1}{d_A^2} \sum_{\substack{\boldsymbol{a},\boldsymbol{a}'\\ \boldsymbol{b},\boldsymbol{b}'}} \prod_{k=0}^{t-1} \mathrm{tr}\left(U_k \left(|a_k\rangle\langle a'_k| \otimes |0\rangle\langle 0|\right) U_k^\dagger \left(\left|a'_{k+1}\right\rangle\!\left\langle a_{k+1}\right| \otimes \left|b'_{k+1}\right\rangle\!\left\langle b_{k+1}\right|\right)\right) \delta_{a_t,a'_t} \prod_{k=0}^{t-1} \delta_{b_{k+1},b'_{k+1}} \\
&\qquad \times \sum_{\substack{\boldsymbol{\alpha},\boldsymbol{\alpha}'\\ \boldsymbol{\beta},\boldsymbol{\beta}'}} \prod_{k=0}^{t-1} \mathrm{tr}\left(U_k \left(|\alpha_k\rangle\langle \alpha'_k| \otimes |0\rangle\langle 0|\right) U_k^\dagger \left(\left|\alpha'_{k+1}\right\rangle\!\left\langle \alpha_{k+1}\right| \otimes \left|\beta'_{k+1}\right\rangle\!\left\langle \beta_{k+1}\right|\right)\right) \delta_{\alpha_t,\alpha'_t} \prod_{k=0}^{t-1} \delta_{\beta_{k+1},\beta'_{k+1}} \delta_{a_0,\alpha'_0} \delta_{a'_0,\alpha_0}
\end{aligned} \tag{E10}$$

$$\begin{aligned}
&= \frac{1}{d_A^2} \sum_{\substack{\boldsymbol{a},\boldsymbol{a}'\\ \boldsymbol{b},\boldsymbol{b}'}} \sum_{\substack{\boldsymbol{\alpha},\boldsymbol{\alpha}'\\ \boldsymbol{\beta},\boldsymbol{\beta}'}} \prod_{k=0}^{t-1} \mathrm{tr}\left(U_k^{\otimes 2} \left(|a_k\alpha_k\rangle\langle a'_k\alpha'_k| \otimes |0\rangle\langle 0|^{\otimes 2}\right) U_k^{\dagger\otimes 2} \left(\left|a'_{k+1}\alpha'_{k+1}\right\rangle\!\left\langle a_{k+1}\alpha_{k+1}\right| \otimes \left|b'_{k+1}\beta'_{k+1}\right\rangle\!\left\langle b_{k+1}\beta_{k+1}\right|\right)\right) \\
&\qquad \times \delta_{a_0,\alpha'_0} \delta_{a'_0,\alpha_0} \delta_{a_t,a'_t} \delta_{\alpha_t,\alpha'_t} \prod_{k=0}^{t-1} \delta_{b_{k+1},b'_{k+1}} \delta_{\beta_{k+1},\beta'_{k+1}},
\end{aligned} \tag{E11}$$

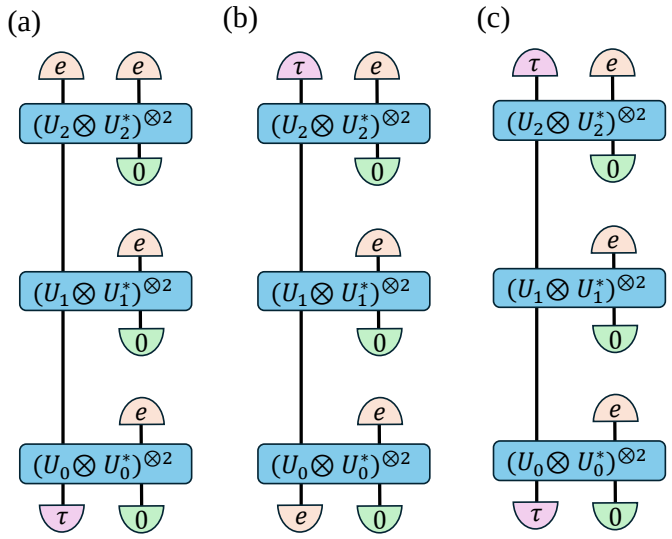

Figure 16. Tensor network representation of Haar-averaged purity for reduced states (a) ρ_R, (b) ρ_{A_t} and (c) ρ_{RA_t} with zero-state reset and time steps $t = 3$.

which can be equivalently expressed in the diagram shown in Fig. 16a with a choice of $t = 3$.

For Haar ensemble average of unitary twirling over two replicas, we have

$$\mathbb{E}_{\text{Haar}}\left[U^{\otimes 2} \otimes U^{*\otimes 2}\right] = \frac{1}{d^2-1}\left[|e)(e| - \frac{1}{d}|e)(\tau| + |\tau)(\tau| - \frac{1}{d}|\tau)(e|\right], \tag{E12}$$

where $|e)$ and $|\tau)$ are the vectorized operator for identity and transposition between two replicas, following the convention of Ref. [7, 45]. The inner product of any two operator thus can be conveniently represented as $\text{tr}\left(A^\dagger B\right) = (A|B)$. The unitary twirling on the step t becomes

$$\begin{aligned}
&\mathbb{E}_{\text{Haar}}\left[U_{t-1}^{\otimes 2} \otimes U_{t-1}^{*\otimes 2}\right] |e)_A|e)_B \\
&= \frac{1}{d_A^2 d_B^2 - 1}\left[d_A^2 d_B^2 |e)_{AB} - |e)_{AB} + d_A d_B |\tau)_{AB} - d_A d_B |\tau)_{AB}\right] &\text{(E13)}\\
&= |e)_{AB}, &\text{(E14)}
\end{aligned}$$

where we utilize $(e|e)_A = d_A^2, (\tau|e)_A = d_A$ in the second line. Via the reseting with $(0|_B$ and replacing it to $|e)_B$ in the $t-1$ step, we reobtain the initial boundary condition $|e)_A|e)_B$. Therefore, the Haar-averaged purity becomes

$$\mathbb{E}_{\text{Haar}}\,\text{tr}\left(\rho_R^2\right) = \frac{1}{d_A^2}(\tau|_A(0|_B|e)_A|e)_B = \frac{1}{d_A}. \tag{E15}$$

Next, we move to the reduced state ρ_{A_t}. Following Eq. (E6), we have

$$\begin{aligned}
&\rho_{A_t} = \text{tr}_{R\boldsymbol{B}}(\rho_{RA_t\boldsymbol{B}}) &\text{(E16)}\\
&= \frac{1}{d_A}\sum_{\substack{\boldsymbol{a},\boldsymbol{a}'\\ \boldsymbol{b},\boldsymbol{b}'}}\prod_{k=0}^{t-1}\text{tr}\left(U_k\left(|a_k\rangle\langle a_k'| \otimes |0\rangle\langle 0|\right)U_k^\dagger\left(\left|a_{k+1}'\right\rangle\left\langle a_{k+1}\right| \otimes \left|b_{k+1}'\right\rangle\left\langle b_{k+1}\right|\right)\right)\delta_{a_0,a_0'}\,|a_t\rangle\langle a_t'|_{A_t}\prod_{k=0}^{t-1}\delta_{b_{k+1},b_{k+1}'}, &\text{(E17)}
\end{aligned}$$

and the purity becomes

$$\begin{aligned}
&\text{tr}\left(\rho_{A_t}^2\right)\\
&= \frac{1}{d_A^2}\sum_{\substack{\boldsymbol{a},\boldsymbol{a}'\\ \boldsymbol{b},\boldsymbol{b}'}}\sum_{\substack{\boldsymbol{\alpha},\boldsymbol{\alpha}'\\ \boldsymbol{\beta},\boldsymbol{\beta}'}}\prod_{k=0}^{t-1}\text{tr}\left(U_k^{\otimes 2}\left(|a_k\alpha_k\rangle\langle a_k'\alpha_k'| \otimes |0\rangle\langle 0|^{\otimes 2}\right)U_k^{\dagger\otimes 2}\left(\left|a_{k+1}'\alpha_{k+1}'\right\rangle\left\langle a_{k+1}\alpha_{k+1}\right| \otimes \left|b_{k+1}'\beta_{k+1}'\right\rangle\left\langle b_{k+1}\beta_{k+1}\right|\right)\right)\\
&\qquad \times \delta_{a_0,a_0'}\delta_{\alpha_0,\alpha_0'}\delta_{a_t,\alpha_t'}\delta_{a_t',\alpha_t}\prod_{k=0}^{t-1}\delta_{b_{k+1},b_{k+1}'}\delta_{\beta_{k+1},\beta_{k+1}'}, &\text{(E18)}
\end{aligned}$$

which is equivalently expressed in the diagram shown in Fig. 16b. The Haar ensemble average from step t is

$$\begin{aligned}
&\mathbb{E}_{\text{Haar}}\left[U_{t-1}^{\otimes 2}\otimes {U_{t-1}^{*}}^{\otimes 2}\right]|\tau)_A|e)_B \\
&=\frac{1}{d_A^2d_B^2-1}\left[d_Ad_B^2|e)-\frac{d_A^2d_B}{d_Ad_B}|e)+d_A^2d_B|\tau)-\frac{d_Ad_B^2}{d_Ad_B}|\tau)\right] &\text{(E19)}\\
&=\frac{d_A(d_B^2-1)}{d_A^2d_B^2-1}|e)_{AB}+\frac{d_B(d_A^2-1)}{d_A^2d_B^2-1}|\tau)_{AB}, &\text{(E20)}
\end{aligned}$$

where in the second line we utilize the fact $(\tau|\tau)_A=d_A^2$. Catenating with $|e)(0|_B$ results in

$$|e)(0|_B\,\mathbb{E}_{\text{Haar}}\left[U_{t-1}^{\otimes 2}\otimes {U_{t-1}^{*}}^{\otimes 2}\right]|\tau)_A|e)_B=\frac{d_A(d_B^2-1)}{d_A^2d_B^2-1}|e)_A|e)_B+\frac{d_B(d_A^2-1)}{d_A^2d_B^2-1}|\tau)_A|e)_B. \tag{E21}$$

We can find that the second term shares the same boundary condition $|\tau)_A|e)_B$ as the step t we have evaluated, and from the calculation in Eq. (E14) we know that the boundary $|e)_A|e)_B$ remains the same through unitary twirling. Therefore, we can separately evaluate the contribution from $|\tau)_A|e)_B$ and $|e)_A|e)_B$ as follows.

- $|\tau)_A|e)_B$:

$$\frac{1}{d_A^2}\left(\frac{d_B(d_A^2-1)}{d_A^2d_B^2-1}\right)^t(e|\tau)_A(0|e)_B=\frac{1}{d_A}\left(\frac{d_B(d_A^2-1)}{d_A^2d_B^2-1}\right)^t. \tag{E22}$$

- $|e)_A|e)_B$:

$$\frac{1}{d_A^2}\frac{d_A(d_B^2-1)}{d_A^2d_B^2-1}\sum_{k=0}^{t-1}\left(\frac{d_B(d_A^2-1)}{d_A^2d_B^2-1}\right)^k(e|e)_A(0|e)_B=\frac{d_A(d_B+1)}{d_A^2d_B+1}\left(1-\left(\frac{d_B(d_A^2-1)}{d_A^2d_B^2-1}\right)^t\right). \tag{E23}$$

Combining the above two terms together, we obtain the dynamical solution of Haar-averaged purity for ρ_{A_t}

$$\begin{aligned}
\mathbb{E}_{\text{Haar}}\,\text{tr}\big(\rho_{A_t}^2\big)&=\frac{1}{d_A}\left(\frac{d_B(d_A^2-1)}{d_A^2d_B^2-1}\right)^t+\frac{d_A(d_B+1)}{d_A^2d_B+1}\left(1-\left(\frac{d_B(d_A^2-1)}{d_A^2d_B^2-1}\right)^t\right) &\text{(E24)}\\
&=\frac{d_A(1+d_B)}{1+d_A^2d_B}+\frac{1-d_A^2}{d_A(1+d_A^2d_B)}\left(\frac{d_B(d_A^2-1)}{d_A^2d_B^2-1}\right)^t. &\text{(E25)}
\end{aligned}$$

Finally, we move to the reduced state ρ_{RA_t}.

$$\begin{aligned}
&\rho_{RA_t}=\text{tr}_{\boldsymbol{B}}(\rho_{RA_t\boldsymbol{B}}) &\text{(E26)}\\
&=\frac{1}{d_A}\sum_{\substack{\boldsymbol{a},\boldsymbol{a}'\\ \boldsymbol{b},\boldsymbol{b}'}}\prod_{k=0}^{t-1}\text{tr}\left(U_k\left(|a_k\rangle\langle a_k'|\otimes|0\rangle\langle 0|\right)U_k^\dagger\left(\left|a_{k+1}'\right\rangle\left\langle a_{k+1}\right|\otimes\left|b_{k+1}'\right\rangle\left\langle b_{k+1}\right|\right)\right)\left(|a_0\rangle\langle a_0'|_R\otimes|a_t\rangle\langle a_t'|_{A_t}\right)\prod_{k=0}^{t-1}\delta_{b_{k+1},b_{k+1}'}, &\text{(E27)}
\end{aligned}$$

and the purity becomes

$$\begin{aligned}
&\text{tr}\big(\rho_{RA_t}^2\big)\\
&=\frac{1}{d_A^2}\sum_{\substack{\boldsymbol{a},\boldsymbol{a}'\\ \boldsymbol{b},\boldsymbol{b}'}}\sum_{\substack{\boldsymbol{\alpha},\boldsymbol{\alpha}'\\ \boldsymbol{\beta},\boldsymbol{\beta}'}}\prod_{k=0}^{t-1}\text{tr}\left(U_k^{\otimes 2}\left(|a_k\alpha_k\rangle\langle a_k'\alpha_k'|\otimes|0\rangle\langle 0|^{\otimes 2}\right)U_k^{\dagger\otimes 2}\left(\left|a_{k+1}'\alpha_{k+1}'\right\rangle\left\langle a_{k+1}\alpha_{k+1}\right|\otimes\left|b_{k+1}'\beta_{k+1}'\right\rangle\left\langle b_{k+1}\beta_{k+1}\right|\right)\right)\\
&\qquad\times\delta_{a_0,\alpha_0'}\delta_{a_0',\alpha_0}\delta_{a_t,\alpha_t'}\delta_{a_t',\alpha_t}\prod_{k=0}^{t-1}\delta_{b_{k+1},b_{k+1}'}\delta_{\beta_{k+1},\beta_{k+1}'}, &\text{(E28)}
\end{aligned}$$

which is equivalently expressed in the diagram shown in Fig. 16c. Since it shares the same boundary condition as in Fig. 16b, we thus can directly write out the contributions from $|\tau)_A|e)_B$ and $|e)_A|e)_B$ as

- $|\tau)_A|e)_B$:

$$\frac{1}{d_A^2}\left(\frac{d_B(d_A^2-1)}{d_A^2d_B^2-1}\right)^t(\tau|\tau)_A(0|e)_B=\left(\frac{d_B(d_A^2-1)}{d_A^2d_B^2-1}\right)^t. \tag{E29}$$

- $|e)_A|e)_B$:

$$\frac{1}{d_A^2}\frac{d_A(d_B^2-1)}{d_A^2d_B^2-1}\sum_{k=0}^{t-1}\left(\frac{d_B(d_A^2-1)}{d_A^2d_B^2-1}\right)^k(\tau|e)_A(0|e)_B=\frac{d_B+1}{d_A^2d_B+1}\left(1-\left(\frac{d_B(d_A^2-1)}{d_A^2d_B^2-1}\right)^t\right). \tag{E30}$$

The dynamical solution of Haar-averaged purity for ρ_{RA_t} becomes

$$\mathbb{E}_{\text{Haar}}\operatorname{tr}\left(\rho_{RA_t}^2\right)=\left(\frac{d_B(d_A^2-1)}{d_A^2d_B^2-1}\right)^t+\frac{d_B+1}{d_A^2d_B+1}\left(1-\left(\frac{d_B(d_A^2-1)}{d_A^2d_B^2-1}\right)^t\right) \tag{E31}$$

$$=\frac{1+d_B}{1+d_A^2d_B}+\frac{d_B(d_A^2-1)}{1+d_A^2d_B}\left(\frac{d_B(d_A^2-1)}{d_A^2d_B^2-1}\right)^t. \tag{E32}$$

To evaluate the Haar-averaged of measurement-uncondioned Rényi-extended QMI in Eq. (5), we switch the order of ensemble average and logarithmic, which does not change the final result as long as the fluctuation of entropy is small. Combining the results in Eqs. (E15), (E25) and (E32), we have

$$\mathbb{E}_{\text{Haar}}\,I_2(R:A_t)\simeq-\log_2\mathbb{E}_{\text{Haar}}\operatorname{tr}\left(\rho_R^2\right)-\log_2\mathbb{E}_{\text{Haar}}\operatorname{tr}\left(\rho_{A_t}^2\right)+\log_2\mathbb{E}_{\text{Haar}}\operatorname{tr}\left(\rho_{RA_t}^2\right) \tag{E33}$$

$$=N_A-\log_2\left[\frac{d_A(1+d_B)}{1+d_A^2d_B}+\frac{1-d_A^2}{d_A(1+d_A^2d_B)}\left(\frac{d_B(d_A^2-1)}{d_A^2d_B^2-1}\right)^t\right]+\log_2\left[\frac{1+d_B}{1+d_A^2d_B}+\frac{d_B(d_A^2-1)}{1+d_A^2d_B}\left(\frac{d_B(d_A^2-1)}{d_A^2d_B^2-1}\right)^t\right], \tag{E34}$$

which is the result of Eq. (11) in the main text. Assuming large system size $d_A, d_B \gg 1$, we can perform asymptotic analysis,

$$\mathbb{E}_{\text{Haar}}\,I_2(R:A_t)=N_A-\log_2\left[\frac{d_A^2(1+d_B)+(1-d_A^2)\left(\frac{d_B(d_A^2-1)}{d_A^2d_B^2-1}\right)^t}{d_A(1+d_A^2d_B)}\right]+\log_2\left[\frac{1+d_B+d_B(d_A^2-1)\left(\frac{d_B(d_A^2-1)}{d_A^2d_B^2-1}\right)^t}{1+d_A^2d_B}\right]$$

$$\simeq N_A-\log_2\left(\frac{1}{d_A}-\frac{1}{d_Ad_B}\frac{1}{d_B^t}\right)+\log_2\left(\frac{1}{d_A^2}+\frac{1}{d_B^t}\right) \tag{E35}$$

$$=N_A-\log_2\frac{1}{d_A}\left(1-\frac{1}{d_B^{t+1}}\right)+\log_2\left(\frac{1}{d_A^2}+\frac{1}{d_B^t}\right) \tag{E36}$$

$$\simeq 2N_A-d_B^{-(t+1)}+\log_2\left(d_A^{-2}+d_B^{-t}\right). \tag{E37}$$

For early time $t \ll 2N_A/N_B$, we can further approximate the QMI as

$$\mathbb{E}_{\text{Haar}}\,I_2(R:A_t)\simeq 2N_A-d_B^{-(t+1)}+\log_2\left(d_A^{-2}+d_B^{-t}\right)$$

$$=2N_A-d_B^{-(t+1)}+\log_2 d_B^{-t}\left(1+d_A^{-2}d_B^t\right) \tag{E38}$$

$$\simeq 2N_A-d_B^{-(t+1)}-tN_B+d_A^{-2}d_B^t \tag{E39}$$

$$\simeq 2N_A-tN_B+\mathcal{O}(d_B^t/d_A^2), \tag{E40}$$

which recovers the linear scaling in the main text. On the other hand for late time $t \gg 2N_A/N_B$, with similar approximation method, we have

$$\mathbb{E}_{\text{Haar}}\,I_2(R:A_t)\simeq 2N_A-d_B^{-(t+1)}+\log_2\left(d_A^{-2}+d_B^{-t}\right)$$

$$=2N_A-d_B^{-(t+1)}+\log_2 d_A^{-2}\left(1+d_A^2d_B^{-t}\right) \tag{E41}$$

$$\simeq 2N_A-d_B^{-(t+1)}-2N_A+d_A^2d_B^{-t} \tag{E42}$$

$$=d_A^2d_B^{-t}+\mathcal{O}(d_B^{-(t+1)}). \tag{E43}$$

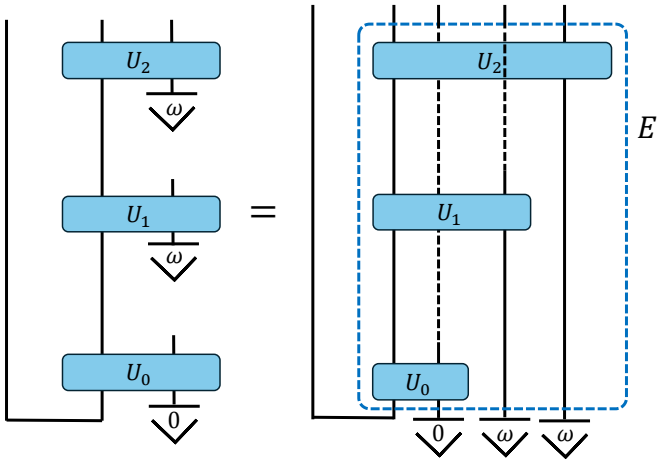

Figure 17. Equivalent relation on the quantum dynamics with mid-circuit measurements and diagonal-mixed-state reset via expanding the bath. Here $\omega = \boldsymbol{I}_B/d_B$ represents the fully-mixed state. The linear map E (blue box) is applied on the initial maximally entangled state. The dashed lines indicate that those outputs do not interact with the unitaries to be passed through. Here we show an example for $t = 3$.

2. Fully-mixed state reset strategy

In this part, we focus on a different reset strategy, the bath system is initialized with a fully-mixed state $\omega = \boldsymbol{I}_B/d_B$ starting from the second step.

Similar to the derivation in pure-state reset strategy, we first write out the linear map E (shown by blue box in Fig. 17) as

$$E = \sum_{\boldsymbol{a},\boldsymbol{b}} \prod_{k=0}^{t-1} \langle a_{k+1} b_{2k+1}|U_k|a_k b_{2k}\rangle \, |a_t\rangle_{A_t} \langle a_0|_{A_0} \otimes_{k=0}^{t-1} |b_{2k+1}\rangle\langle b_{2k}| \,, \tag{E44}$$

where different from above we define the vector representation $\boldsymbol{b} = (b_0, b_1, \cdots, b_{2t-2}, b_{2t-1})$. Via applying the linear map E on maximally entangled state $|\Phi\rangle_{RA_0}$ and the expanded bath system (shown in Fig. 17), we have the output state over the whole system as

$$\rho_{RA_t\boldsymbol{B}} = (\mathbb{I}_R \otimes E)\left(|\Phi\rangle\langle\Phi|_{RA_0} \left(\otimes_{k=0}^{t-1}\omega\right) \otimes |0\rangle\langle 0|\right)(\mathbb{I}_R \otimes E)^\dagger \tag{E45}$$

$$= \frac{1}{d_A} \sum_{\substack{\boldsymbol{a},\boldsymbol{b},\\ \boldsymbol{a}',\boldsymbol{b}'}} \prod_{k=0}^{t-1} \langle a_{k+1} b_{2k+1}|U_k|a_k b_{2k}\rangle \, \langle a'_k b'_{2k}|U_k^\dagger|a'_{k+1} b'_{2k+1}\rangle \, |a_0\rangle\langle a'_0|_R \, |a_t\rangle\langle a'_t|_{A_t} \left(\otimes_{k=0}^{t-1} |b_{2k+1}\rangle\langle b'_{2k+1}|\right) \langle b_0|0\rangle \, \langle 0|b'_0\rangle \otimes_{k=1}^{t-1} \langle b_{2k}|\omega|b'_{2k}\rangle \tag{E46}$$

$$= \frac{1}{d_A}\frac{1}{d_B^{t-1}} \sum_{\substack{\boldsymbol{a},\boldsymbol{b},\\ \boldsymbol{a}',\boldsymbol{b}'}} \prod_{k=0}^{t-1} \langle a_{k+1} b_{2k+1}|U_k|a_k b_{2k}\rangle \, \langle a'_k b'_{2k}|U_k^\dagger|a'_{k+1} b'_{2k+1}\rangle \, |a_0\rangle\langle a'_0|_R \, |a_t\rangle\langle a'_t|_{A_t} \left(\otimes_{k=0}^{t-1} |b_{2k+1}\rangle\langle b'_{2k+1}|\right) \delta_{b_0,0}\delta_{b'_0,0} \prod_{k=1}^{t-1} \delta_{b_{2k},b'_{2k}}. \tag{E47}$$

For the reduced state ρ_R, we have

$$\rho_R = \mathrm{tr}_{A_t\boldsymbol{B}}(\rho_{RA_t\boldsymbol{B}}) \tag{E48}$$

$$= \frac{1}{d_A}\frac{1}{d_B^{t-1}} \sum_{\substack{\boldsymbol{a},\boldsymbol{b},\\ \boldsymbol{a}',\boldsymbol{b}'}} \prod_{k=0}^{t-1} \langle a_{k+1}b_{2k+1}|U_k|a_kb_{2k}\rangle \langle a'_kb'_{2k}|U_k^\dagger|a'_{k+1}b'_{2k+1}\rangle |a_0\rangle\langle a'_0|_R \,\delta_{a_t,a'_t} \prod_{k=0}^{t-1} \delta_{b_{2k+1},b'_{2k+1}}\delta_{b_0,0}\delta_{b'_0,0} \prod_{k=1}^{t-1}\delta_{b_{2k},b'_{2k}} \tag{E49}$$

$$= \frac{1}{d_A}\frac{1}{d_B^{t-1}} \sum_{\boldsymbol{a},\boldsymbol{a}'} \prod_{k=1}^{t-1} \mathrm{tr}\left(U_k\left(|a_k\rangle\langle a'_k|\otimes \boldsymbol{I}\right)U_k^\dagger\left(|a'_{k+1}\rangle\langle a_{k+1}|\otimes \boldsymbol{I}\right)\right)\mathrm{tr}\left(U_0\left(|a_0\rangle\langle a'_0|\otimes|0\rangle\langle 0|\right)U_0^\dagger\left(|a'_1\rangle\langle a_1|\otimes \boldsymbol{I}\right)\right)|a_0\rangle\langle a'_0|_R\,\delta_{a_t,a'_t}. \tag{E50}$$

The purity of ρ_R then can be evaluated as

$$\begin{aligned}&\mathrm{tr}\left(\rho_R^2\right)\\ &= \frac{1}{d_A^2}\frac{1}{d_B^{2t-2}} \sum_{\boldsymbol{a},\boldsymbol{a}'} \prod_{k=1}^{t-1} \mathrm{tr}\left(U_k\left(|a_k\rangle\langle a'_k|\otimes \boldsymbol{I}\right)U_k^\dagger\left(|a'_{k+1}\rangle\langle a_{k+1}|\otimes \boldsymbol{I}\right)\right)\mathrm{tr}\left(U_0\left(|a_0\rangle\langle a'_0|\otimes|0\rangle\langle 0|\right)U_0^\dagger\left(|a'_1\rangle\langle a_1|\otimes \boldsymbol{I}\right)\right)\delta_{a_t,a'_t}\\ &\quad\times \sum_{\boldsymbol{\alpha},\boldsymbol{\alpha}'} \prod_{k=1}^{t-1} \mathrm{tr}\left(U_k\left(|\alpha_k\rangle\langle \alpha'_k|\otimes \boldsymbol{I}\right)U_k^\dagger\left(|\alpha'_{k+1}\rangle\langle \alpha_{k+1}|\otimes \boldsymbol{I}\right)\right)\mathrm{tr}\left(U_0\left(|\alpha_0\rangle\langle \alpha'_0|\otimes|0\rangle\langle 0|\right)U_0^\dagger\left(|\alpha'_1\rangle\langle \alpha_1|\otimes \boldsymbol{I}\right)\right)\delta_{\alpha_t,\alpha'_t}\delta_{a_0,\alpha'_0}\delta_{a'_0,\alpha_0}\end{aligned} \tag{E51}$$

$$\begin{aligned}&= \frac{1}{d_A^2}\frac{1}{d_B^{2t-2}} \sum_{\substack{\boldsymbol{a},\boldsymbol{a}',\\ \boldsymbol{\alpha},\boldsymbol{\alpha}'}} \prod_{k=1}^{t-1} \mathrm{tr}\left(U_k^{\otimes 2}\left(|a_k\alpha_k\rangle\langle a'_k\alpha'_k|\otimes \boldsymbol{I}^{\otimes 2}\right)U_k^{\dagger\otimes 2}\left(|a'_{k+1}\alpha'_{k+1}\rangle\langle a_{k+1}\alpha_{k+1}|\otimes \boldsymbol{I}^{\otimes 2}\right)\right)\\ &\quad\times \mathrm{tr}\left(U_0^{\otimes 2}\left(|a_0\alpha_0\rangle\langle a'_0\alpha'_0|\otimes|0\rangle\langle 0|^{\otimes 2}\right)U_0^{\dagger\otimes 2}\left(|a'_1\alpha'_1\rangle\langle a_1\alpha_1|\otimes \boldsymbol{I}^{\otimes 2}\right)\right)\delta_{a_t,a'_t}\delta_{\alpha_t,\alpha'_t}\delta_{a_0,\alpha'_0}\delta_{a'_0,\alpha_0},\end{aligned} \tag{E52}$$

which is represented in tensor network in Fig. 18a.

Recall that $\mathbb{E}_{\mathrm{Haar}}\left[U_{t-1}^{\otimes 2}\otimes {U_{t-1}^*}^{\otimes 2}\right]|e)_A|e)_B = |e)_{AB}$ from Eq. (E14), the following concatenation with $|e)(e|_B$ results in

$$|e)(e|_B\,\mathbb{E}_{\mathrm{Haar}}\left[U_{t-1}^{\otimes 2}\otimes {U_{t-1}^*}^{\otimes 2}\right]|e)_A|e)_B = d_B^2|e)_A|e)_B, \tag{E53}$$

As the boundary condition is exactly reproduced in the following step with an extra coefficient d_B^2, then we can directly obtain the solution of purity as

$$\mathbb{E}_{\mathrm{Haar}}\,\mathrm{tr}\left(\rho_R^2\right) = \frac{1}{d_A^2}\frac{1}{d_B^{2t-2}} d_B^{2(t-1)}(\tau|_A(0|_B|e)_A|e)_B = \frac{1}{d_A}. \tag{E54}$$

Next, we move to the reduced state ρ_{A_t}.

$$\rho_{A_t} = \mathrm{tr}_{R\boldsymbol{B}}(\rho_{RA_t\boldsymbol{B}}) \tag{E55}$$

$$= \frac{1}{d_A}\frac{1}{d_B^{t-1}} \sum_{\substack{\boldsymbol{a},\boldsymbol{b},\\ \boldsymbol{a}',\boldsymbol{b}'}} \prod_{k=0}^{t-1} \langle a_{k+1}b_{2k+1}|U_k|a_kb_{2k}\rangle \langle a'_kb'_{2k}|U_k^\dagger|a'_{k+1}b'_{2k+1}\rangle \,\delta_{a_0,a'_0}\,|a_t\rangle\langle a'_t|_{A_t} \prod_{k=0}^{t-1} \delta_{b_{2k+1},b'_{2k+1}}\delta_{b_0,0}\delta_{b'_0,0} \prod_{k=1}^{t-1}\delta_{b_{2k},b'_{2k}} \tag{E56}$$

$$= \frac{1}{d_A}\frac{1}{d_B^{t-1}} \sum_{\boldsymbol{a},\boldsymbol{a}'} \prod_{k=1}^{t-1} \mathrm{tr}\left(U_k\left(|a_k\rangle\langle a'_k|\otimes \boldsymbol{I}\right)U_k^\dagger\left(|a'_{k+1}\rangle\langle a_{k+1}|\otimes \boldsymbol{I}\right)\right)\mathrm{tr}\left(U_0\left(|a_0\rangle\langle a'_0|\otimes|0\rangle\langle 0|\right)U_0^\dagger\left(|a'_1\rangle\langle a_1|\otimes \boldsymbol{I}\right)\right)\delta_{a_0,a'_0}\,|a_t\rangle\langle a'_t|_{A_t}\,, \tag{E57}$$

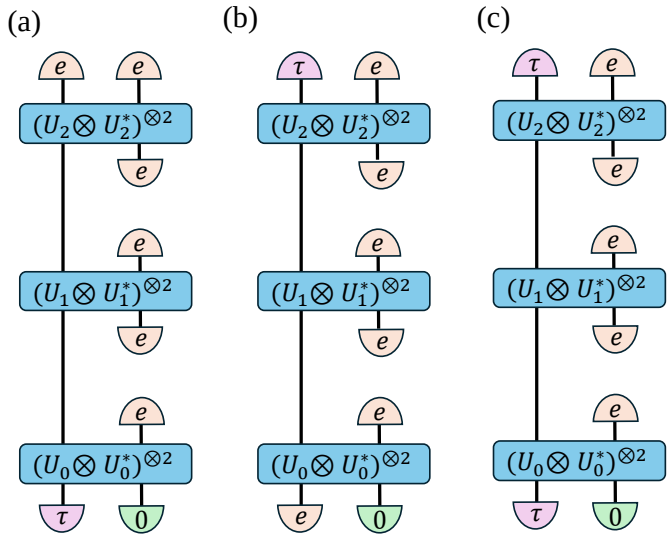

Figure 18. Tensor network representation of Haar-averaged purity for reduced states (a) ρ_R, (b) ρ_{A_t} and (c) ρ_{RA_t} with fully-mixed state reset and time steps $t = 3$.

and the purity is

$$\begin{aligned}
&\mathrm{tr}\left(\rho_{A_t}^2\right) \\
&= \frac{1}{d_A^2}\frac{1}{d_B^{2t-2}} \sum_{\boldsymbol{a},\boldsymbol{a}'} \prod_{k=1}^{t-1} \mathrm{tr}\left(U_k \left(|a_k\rangle\langle a_k'| \otimes \boldsymbol{I}\right) U_k^\dagger \left(|a_{k+1}'\rangle\langle a_{k+1}| \otimes \boldsymbol{I}\right)\right) \mathrm{tr}\left(U_0 \left(|a_0\rangle\langle a_0'| \otimes |0\rangle\langle 0|\right) U_0^\dagger \left(|a_1'\rangle\langle a_1| \otimes \boldsymbol{I}\right)\right) \delta_{a_0,a_0'} \\
&\quad \times \sum_{\boldsymbol{\alpha},\boldsymbol{\alpha}'} \prod_{k=1}^{t-1} \mathrm{tr}\left(U_k \left(|\alpha_k\rangle\langle \alpha_k'| \otimes \boldsymbol{I}\right) U_k^\dagger \left(|\alpha_{k+1}'\rangle\langle \alpha_{k+1}| \otimes \boldsymbol{I}\right)\right) \mathrm{tr}\left(U_0 \left(|\alpha_0\rangle\langle \alpha_0'| \otimes |0\rangle\langle 0|\right) U_0^\dagger \left(|\alpha_1'\rangle\langle \alpha_1| \otimes \boldsymbol{I}\right)\right) \delta_{\alpha_0,\alpha_0'} \delta_{a_t,\alpha_t'} \delta_{a_t',\alpha_t}
\end{aligned} \tag{E58}$$

$$\begin{aligned}
&= \frac{1}{d_A^2}\frac{1}{d_B^{2t-2}} \sum_{\substack{\boldsymbol{a},\boldsymbol{a}', \\ \boldsymbol{\alpha},\boldsymbol{\alpha}'}} \prod_{k=1}^{t-1} \mathrm{tr}\left(U_k^{\otimes 2} \left(|a_k\alpha_k\rangle\langle a_k'\alpha_k'| \otimes \boldsymbol{I}^{\otimes 2}\right) U_k^{\dagger\otimes 2} \left(|a_{k+1}'\alpha_{k+1}'\rangle\langle a_{k+1}\alpha_{k+1}| \otimes \boldsymbol{I}^{\otimes 2}\right)\right) \\
&\quad \times \mathrm{tr}\left(U_0^{\otimes 2} \left(|a_0\alpha_0\rangle\langle a_0'\alpha_0'| \otimes |0\rangle\langle 0|^{\otimes 2}\right) U_0^{\dagger\otimes 2} \left(|a_1'\alpha_1'\rangle\langle a_1\alpha_1| \otimes \boldsymbol{I}^{\otimes 2}\right)\right) \delta_{a_0,a_0'} \delta_{\alpha_0,\alpha_0'} \delta_{a_t,\alpha_t'} \delta_{a_t',\alpha_t},
\end{aligned} \tag{E59}$$

which is shown in Fig. 18b.

Recall from Eq. (E20) $\mathbb{E}_{\mathrm{Haar}}\left[U_{t-1}^{\otimes 2} \otimes {U_{t-1}^*}^{\otimes 2}\right] |\tau\rangle_A |e\rangle_B = \frac{d_A(d_B^2-1)}{d_A^2 d_B^2-1} |e\rangle_{AB} + \frac{d_B(d_A^2-1)}{d_A^2 d_B^2-1} |\tau\rangle_{AB}$, we next apply $|e)(e|_B$ and have

$$|e)(e|_B \, \mathbb{E}_{\mathrm{Haar}}\left[U_{t-1}^{\otimes 2} \otimes {U_{t-1}^*}^{\otimes 2}\right] |\tau\rangle_A |e\rangle_B = \frac{d_A d_B^2 (d_B^2-1)}{d_A^2 d_B^2 - 1} |e\rangle_A |e\rangle_B + \frac{d_B^2 (d_A^2-1)}{d_A^2 d_B^2 - 1} |\tau\rangle_A |e\rangle_B, \tag{E60}$$

Moving downward in Fig. 18b up to U_1, we have the contribution from the two boundary conditions above as

- $|\tau\rangle_A |e\rangle_B$: $\left(\frac{d_B^2(d_A^2-1)}{d_A^2 d_B^2-1}\right)^{t-1} |\tau\rangle_A |e\rangle_B$.

- $|e\rangle_A |e\rangle_B$: $\frac{d_A d_B^2 (d_B^2-1)}{d_A^2 d_B^2-1} \sum_{k=0}^{t-2} \left(\frac{d_B^2(d_A^2-1)}{d_A^2 d_B^2-1}\right)^k d_B^{2(t-2-k)} |e\rangle_A |e\rangle_B$.

After finishing the twirling over U_0, we have the dynamical solution for purity of ρ_{A_t}

$$
\begin{aligned}
&\mathbb{E}_{\text{Haar}}\,\mathrm{tr}\big(\rho_{A_t}^2\big)\\
&=\frac{1}{d_A^2}\frac{1}{d_B^{2(t-1)}}\left[\left(\frac{d_B^2(d_A^2-1)}{d_A^2d_B^2-1}\right)^{t-1}\frac{d_B(d_A^2-1)}{d_A^2d_B^2-1}d_A+\left(\frac{d_B^2(d_A^2-1)}{d_A^2d_B^2-1}\right)^{t-1}\frac{d_A(d_B^2-1)}{d_A^2d_B^2-1}d_A^2\right.\\
&\qquad\left.+\frac{d_Ad_B^2(d_B^2-1)}{d_A^2d_B^2-1}\sum_{k=0}^{t-2}\left(\frac{d_B^2(d_A^2-1)}{d_A^2d_B^2-1}\right)^{k}d_B^{2(t-2-k)}d_A^2\right] &\text{(E61)}\\
&=\frac{1}{d_A^2}\frac{1}{d_B^{2(t-1)}}\left[\frac{d_A}{d_B}\left(\frac{d_B^2(d_A^2-1)}{d_A^2d_B^2-1}\right)^{t}+\frac{d_A^3(d_B^2-1)}{(d_A^2-1)d_B^2}\left(\frac{d_B^2(d_A^2-1)}{d_A^2d_B^2-1}\right)^{t}+\frac{d_Ad_B^{2(t-1)}}{d_A^2-1}\left(d_A^2-1-(d_A^2d_B^2-1)\left(\frac{d_A^2-1}{d_A^2d_B^2-1}\right)^{t}\right)\right] &\text{(E62)}\\
&=\frac{d_B}{d_A}\left(\frac{d_A^2-1}{d_A^2d_B^2-1}\right)^{t}+\frac{d_A(d_B^2-1)}{d_A^2-1}\left(\frac{d_A^2-1}{d_A^2d_B^2-1}\right)^{t}+\frac{1}{d_A(d_A^2-1)}\left(d_A^2-1-(d_A^2d_B^2-1)\left(\frac{d_A^2-1}{d_A^2d_B^2-1}\right)^{t}\right) &\text{(E63)}\\
&=\frac{d_B-1}{d_A}\left(\frac{d_A^2-1}{d_A^2d_B^2-1}\right)^{t}+\frac{1}{d_A}. &\text{(E64)}
\end{aligned}
$$

Last, the reduce state ρ_{RA_t} is

$$
\begin{aligned}
&\rho_{RA_t}=\mathrm{tr}_{\boldsymbol{B}}(\rho_{RA_t\boldsymbol{B}}) &\text{(E65)}\\
&=\frac{1}{d_A}\frac{1}{d_B^{t-1}}\sum_{\substack{\boldsymbol{a},\boldsymbol{b},\\ \boldsymbol{a}',\boldsymbol{b}'}}\prod_{k=0}^{t-1}\langle a_{k+1}b_{2k+1}|U_k|a_kb_{2k}\rangle\,\langle a_k'b_{2k}'|U_k^\dagger|a_{k+1}'b_{2k+1}'\rangle\,|a_0\rangle\langle a_0'|_R\,|a_t\rangle\langle a_t'|_{A_t}\prod_{k=0}^{t-1}\delta_{b_{2k+1},b_{2k+1}'}\delta_{b_0,0}\delta_{b_0',0}\prod_{k=1}^{t-1}\delta_{b_{2k},b_{2k}'} &\text{(E66)}\\
&=\frac{1}{d_A}\frac{1}{d_B^{t-1}}\sum_{\boldsymbol{a},\boldsymbol{a}'}\prod_{k=1}^{t-1}\mathrm{tr}\left(U_k\left(|a_k\rangle\langle a_k'|\otimes\boldsymbol{I}\right)U_k^\dagger\left(\left|a_{k+1}'\right\rangle\left\langle a_{k+1}\right|\otimes\boldsymbol{I}\right)\right)\mathrm{tr}\left(U_0\left(|a_0\rangle\langle a_0'|\otimes|0\rangle\langle 0|\right)U_0^\dagger\left(|a_1'\rangle\langle a_1|\otimes\boldsymbol{I}\right)\right)|a_0\rangle\langle a_0'|_R\,|a_t\rangle\langle a_t'|_{A_t}\,, &\text{(E67)}
\end{aligned}
$$

and the purity is

$$
\begin{aligned}
&\mathrm{tr}\big(\rho_{RA_t}^2\big)\\
&=\frac{1}{d_A^2}\frac{1}{d_B^{2t-2}}\sum_{\boldsymbol{a},\boldsymbol{a}'}\prod_{k=1}^{t-1}\mathrm{tr}\left(U_k\left(|a_k\rangle\langle a_k'|\otimes\boldsymbol{I}\right)U_k^\dagger\left(\left|a_{k+1}'\right\rangle\left\langle a_{k+1}\right|\otimes\boldsymbol{I}\right)\right)\mathrm{tr}\left(U_0\left(|a_0\rangle\langle a_0'|\otimes|0\rangle\langle 0|\right)U_0^\dagger\left(|a_1'\rangle\langle a_1|\otimes\boldsymbol{I}\right)\right)\delta_{a_0,\alpha_0'}\delta_{a_0',\alpha_0}\\
&\qquad\times\sum_{\boldsymbol{\alpha},\boldsymbol{\alpha}'}\prod_{k=1}^{t-1}\mathrm{tr}\left(U_k\left(|\alpha_k\rangle\langle\alpha_k'|\otimes\boldsymbol{I}\right)U_k^\dagger\left(\left|\alpha_{k+1}'\right\rangle\left\langle\alpha_{k+1}\right|\otimes\boldsymbol{I}\right)\right)\mathrm{tr}\left(U_0\left(|\alpha_0\rangle\langle\alpha_0'|\otimes|0\rangle\langle 0|\right)U_0^\dagger\left(|\alpha_1'\rangle\langle\alpha_1|\otimes\boldsymbol{I}\right)\right)\delta_{a_t,\alpha_t'}\delta_{a_t',\alpha_t} &\text{(E68)}\\
&=\frac{1}{d_A^2}\frac{1}{d_B^{2t-2}}\sum_{\substack{\boldsymbol{a},\boldsymbol{a}',\\ \boldsymbol{\alpha},\boldsymbol{\alpha}'}}\prod_{k=1}^{t-1}\mathrm{tr}\left(U_k^{\otimes 2}\left(|a_k\alpha_k\rangle\langle a_k'\alpha_k'|\otimes\boldsymbol{I}^{\otimes 2}\right)U_k^{\dagger\otimes 2}\left(\left|a_{k+1}'\alpha_{k+1}'\right\rangle\left\langle a_{k+1}\alpha_{k+1}\right|\otimes\boldsymbol{I}^{\otimes 2}\right)\right)\\
&\qquad\times\mathrm{tr}\left(U_0^{\otimes 2}\left(|a_0\alpha_0\rangle\langle a_0'\alpha_0'|\otimes|0\rangle\langle 0|^{\otimes 2}\right)U_0^{\dagger\otimes 2}\left(|a_1'\alpha_1'\rangle\langle a_1\alpha_1|\otimes\boldsymbol{I}^{\otimes 2}\right)\right)\delta_{a_0,\alpha_0'}\delta_{a_0',\alpha_0}\delta_{a_t,\alpha_t'}\delta_{a_t',\alpha_t}, &\text{(E69)}
\end{aligned}
$$

which is represented as tensor network as in Fig. 18c. Since it shares the same boundary condition as in Fig. 18b, the

contribution toward U_1 remains the same as in $\mathrm{tr}(\rho_{A_t}^2)$. The dynamical solution for the purity of ρ_{RA_t} is

$$\begin{aligned}
&\mathbb{E}_{\mathrm{Haar}}\,\mathrm{tr}\left(\rho_{RA_t}^2\right)\\
&=\frac{1}{d_A^2}\frac{1}{d_B^{2(t-1)}}\left[\left(\frac{d_B^2(d_A^2-1)}{d_A^2d_B^2-1}\right)^{t-1}\frac{d_B(d_A^2-1)}{d_A^2d_B^2-1}d_A^2+\left(\frac{d_B^2(d_A^2-1)}{d_A^2d_B^2-1}\right)^{t-1}\frac{d_A(d_B^2-1)}{d_A^2d_B^2-1}d_A\right.\\
&\qquad\left.+\frac{d_A(d_B^2-1)}{d_A^2d_B^2-1}d_B^{2(t-1)}\sum_{k=0}^{t-2}\left(\frac{d_B^2(d_A^2-1)}{d_A^2d_B^2-1}\right)^k d_B^{-2k}d_A\right] &\text{(E70)}\\
&=\frac{1}{d_A^2}\frac{1}{d_B^{2(t-1)}}\left[\frac{d_A^2}{d_B}\left(\frac{d_B^2(d_A^2-1)}{d_A^2d_B^2-1}\right)^t+\frac{d_A^2(d_B^2-1)}{(d_A^2-1)d_B^2}\left(\frac{d_B^2(d_A^2-1)}{d_A^2d_B^2-1}\right)^t+\frac{d_B^{2(t-1)}}{d_A^2-1}\left(d_A^2-1-(d_A^2d_B^2-1)\left(\frac{d_A^2-1}{d_A^2d_B^2-1}\right)^t\right)\right] &\text{(E71)}\\
&=\left(d_B-\frac{1}{d_A^2}\right)\left(\frac{d_A^2-1}{d_A^2d_B^2-1}\right)^t+\frac{1}{d_A^2}. &\text{(E72)}
\end{aligned}$$

We again switch the order of ensemble average and logarithmic, and combine the results in Eqs. (E54), (E64) and (E72).

$$\begin{aligned}
\mathbb{E}_{\mathrm{Haar}}\,I_2(R:A_t)&\simeq-\log_2\mathbb{E}_{\mathrm{Haar}}\,\mathrm{tr}\left(\rho_R^2\right)-\log_2\mathbb{E}_{\mathrm{Haar}}\,\mathrm{tr}\left(\rho_{A_t}^2\right)+\log_2\mathbb{E}_{\mathrm{Haar}}\,\mathrm{tr}\left(\rho_{RA_t}^2\right) &\text{(E73)}\\
&=N_A-\log_2\left[\frac{d_B-1}{d_A}\left(\frac{d_A^2-1}{d_A^2d_B^2-1}\right)^t+\frac{1}{d_A}\right]+\log_2\left[\left(d_B-\frac{1}{d_A^2}\right)\left(\frac{d_A^2-1}{d_A^2d_B^2-1}\right)^t+\frac{1}{d_A^2}\right], &\text{(E74)}
\end{aligned}$$

which is the result of Eq. (31) in the main text. In the large limit of system $d_A, d_B \gg 1$, we perform the asymptotic analysis as

$$\begin{aligned}
\mathbb{E}_{\mathrm{Haar}}\,I_2(R:A_t)&\simeq N_A-\log_2\left(\frac{1}{d_A}d_B^{1-2t}+\frac{1}{d_A}\right)+\log_2\left(d_B^{1-2t}+\frac{1}{d_A^2}\right) &\text{(E75)}\\
&\simeq 2N_A-d_B^{1-2t}+\log_2\left(d_A^{-2}+d_B^{1-2t}\right). &\text{(E76)}
\end{aligned}$$

In the early time $t \ll N_A/N_B + 1/2$, we can further approximate it as

$$\begin{aligned}
\mathbb{E}_{\mathrm{Haar}}\,I_2(R:A_t)&\simeq 2N_A-d_B^{1-2t}+\log_2 d_B^{1-2t}\left(d_A^{-2}d_B^{2t-1}+1\right) &\text{(E77)}\\
&\simeq 2N_A-d_B^{1-2t}+(1-2t)N_B+d_A^{-2}d_B^{2t-1} &\text{(E78)}\\
&\simeq 2N_A+N_B-2tN_B+\mathcal{O}(d_B^{1-2t}). &\text{(E79)}
\end{aligned}$$

While for the late time $t \gg N_A/N_B + 1/2$, we can further approximate it as

$$\begin{aligned}
\mathbb{E}_{\mathrm{Haar}}\,I_2(R:A_t)&\simeq 2N_A-d_B^{1-2t}+\log_2 d_A^{-2}\left(1+d_A^2d_B^{1-2t}\right) &\text{(E80)}\\
&\simeq 2N_A-d_B^{1-2t}-2N_A+d_A^2d_B^{1-2t} &\text{(E81)}\\
&\simeq d_A^2d_B^{1-2t}. &\text{(E82)}
\end{aligned}$$

Appendix F: Additional numerical details

In this section, we provide additional numerical simulation results to support the theorems and estimation of lifetime in the main text. We simulate the dynamics of QMI with `TensorCircuit` [46].

In Fig. 19a-b, we show the decay of normalized measurement-conditioned QMI versus a rescaled time $(1-1/d_B)t+1$ in various data system N_A with either randomly sampled or identical unitary from Haar ensemble. With increasing N_A, we clearly see a logarithmic decay, and thus can estimate the corresponding QMI lifetime via a threshold (i.e. $\epsilon = 1/4$). Similar observations are also found for Hamiltonian evolution (shown in Fig. 20). In main text, we only show the asymptotic lower bound of Eq. (D68) (red), here we compare it to the complete form of Eq. (D62) (green) in Fig. 19c. In fact, in the most valid range of decay, the two bounds overlap and align with the numerical results. Moreover, through a comparison to the numerical simulation of lower bound Eq. (D5) in derivation, we find that in early stage our theoretical results of either Eq. (D62) or Eq. (D68) agree well, and the deviation to the simulation of QMI (blue) is due to the difference between von Neumann entropy and its Rényi counterpart.

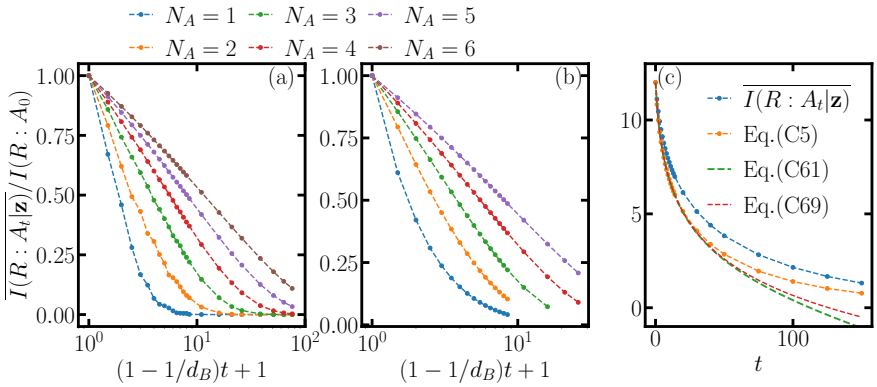

Figure 19. Dynamics of normalized measurement-conditioned QMI $\overline{I(R:A_t|\mathbf{z})}$ with mid-circuit measurements and reset. In (a) and (b) we plot QMI with different data system N_A and same bath $N_B = 1$ with randomly sampled unitary and identical unitary from Haar ensemble through different steps. In (c), dots are numerical simulation results of $\overline{I(R:A_t|\mathbf{z})}$ with $N_A = 5$ (same as purple in (a)). Orange dashed line represent numerical results of the lower bound in Eq. (D5). Green and red dashed lines show Orange and green dashed line represent the theoretical lower bounds Eq. (D62) and Eq. (D68).

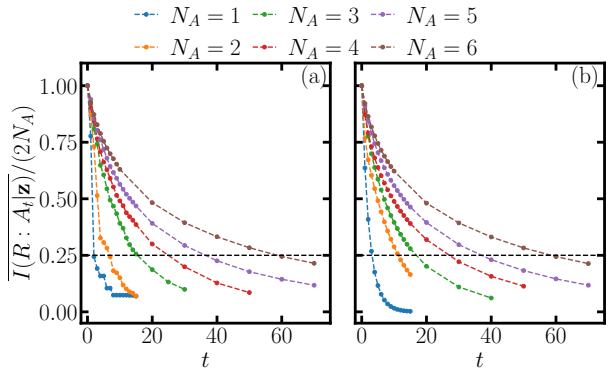

Figure 20. Dynamics of normalized measurement-conditioned QMI $\overline{I(R:A_t|\mathbf{z})}$ with mid-circuit measurements and reset. In (a) and (b) we plot QMI with different data system N_A and same bath $N_B = 1$ with Hamiltonian evolution with randomly sampled coefficients and identical Hamiltonian evolution.

For measurement-unconditioned QMI, as shown in Fig. 21 we still see that with increasing system size N_A, the dynamics of QMI behaves similarly as a linear decay for all possible four unitary settings under consideration. Therefore, we can estimate the corresponding QMI lifetime from numerical simulation of dynamics and we present the results in the main text and Appendix. B.

In Fig. 22b1-b5, we show the normalized bipartite entanglement entropy $S_{\text{half}}/(N_A + N_B)$ of eigenstates of the Ising Hamiltonian in Eq. (7) with different N_A and $N_B = 2$. Since we only find the thermalized state entanglement spectrums, there does not exist "many-body scar" signature in the Hamiltonian considered here. Moreover, we evaluate the projection overlap between each eigenstate $|E_j\rangle$ and representative eigenstates of quantum channel $\mathcal{P}_0$ appended with $|0\rangle\langle 0|_B$ on bath. For a fair comparison, we normalize the norm of overlap and plot it versus normalized eigenenergies E_j for different N_A in Fig. 22c1-c5. For the fixed state (blue) and second largest eigenstate (green), the largest overlaps with Hamiltonian eigenstates lies at the boundaries, corresponding to eigenstates with nearly zero bipartite entanglement. In contrast, for $\sigma_|$ (orange), the operator with medium eigenvalue norm $|\lambda_{\text{mid}}|$ from spectrum $\mathcal{P}_0$, the major contribution on overlap comes from thermalized Hamiltonian eigenstates instead of the boundary parts. For visualization convenience, we mark the corresponding eigenvalues of $\rho_{\text{fix}}, \sigma_1, \sigma_{\text{mid}}$ in Fig. 22a1-a5.

Appendix G: Details of QMI dynamics simulation on quantum hardware

In this section, we provide detail to the simulation of QMI dynamics on the IBM Quantum devices. To mimic the Haar random unitaries concerned in the theoretical studies, we implement the fast scrambling model in each step for the gate-based circuit with appropriate modifications detailed as follows. In a system of N qubits, the original fast

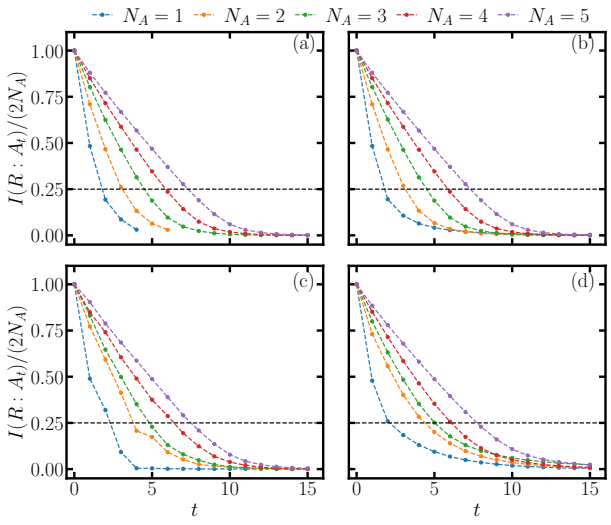

Figure 21. Dynamics of normalized measurement-unconditioned QMI $I(R:A_t)$ with mid-circuit measurements and reset. We plot QMI with different data system N_A and same bath $N_B = 1$ with (a) randomly sampled Haar unitary (b) identical Haar unitary, (c) Hamiltonian evolution with random coefficients and (d) identical Hamiltonian evolution.

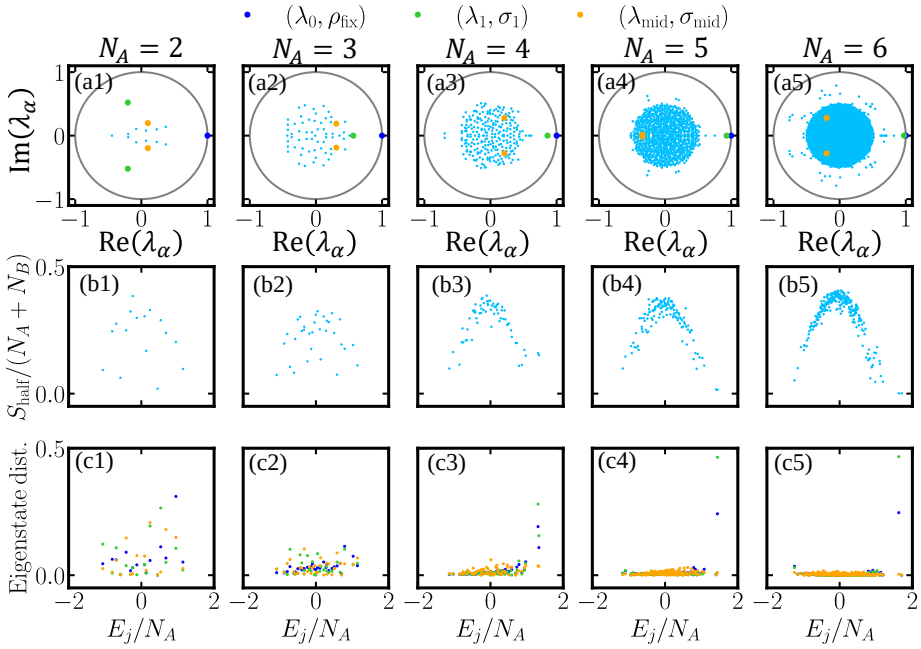

Figure 22. (a1)-(a5) Eigenspectrum of $\mathcal{P}_0$. Blue, green and orange dots indicate the eigenstates $\rho_{\text{fix}}, \sigma_1, \sigma_{\text{mid}}$ to be considered. (b1)-(b5) Normalized bipartite entanglement entropy of Hamiltonian H eigenstates versus normalized eigenenergies. (c1)-(c5) Normalized norm of overlap between eigenstates of $\mathcal{P}_0$ and eigenstates of Hamiltonian versus normalized eigenenergies. In all cases, we have bath $N_B = 2$.

scrambling model [40] is defined as

$$U = \prod_{\ell=1}^{L} \left(e^{-i\frac{g}{2\sqrt{N}} \sum_{i<j} Z_i Z_j} \right) \left(\otimes_{i=1}^{N} V_i^{(\ell)} \right), \tag{G1}$$

where $V_i^{(\ell)}$ is single qubit unitaries randomly sampled from Haar ensemble, and the entangling layer involves ZZ rotation between every pair of qubits. In consideration of the device we simulate, IBM Sherbrooke, can only perform

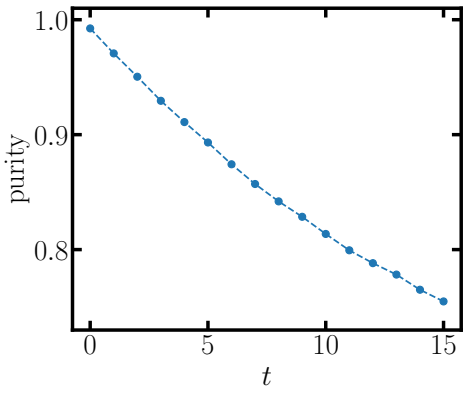

Figure 23. Purity of post-measurement conditional state at different time steps in noisy simulation. Here we perform simulation on a system of $N_A = 3, N_B = 1$ qubits with FSA consisting of $L = 2$ layers, and 1024 shots for mid-circuit measurements on the bath system. Each dot is averaged over 10 randomized circuits.

RZ gate, SX gate, Pauli-X gate and echoed cross-resonance (ECR) gate natively, we therefore replace ZZ-rotation gates in the above original fast scrambling model to ECR gate as

$$U_{\text{simu}} = \prod_{\ell=1}^{L} \left(\prod_{i<j} \text{ECR}_{ij} \right) \left(\otimes_{i=1}^{N} V_i^{(\ell)} \right), \tag{G2}$$

where $\text{ECR}_{ij} \equiv \frac{1}{\sqrt{2}}(\boldsymbol{I}_i \otimes X_j - X_i \otimes Y_j)$ with X_i, Y_j denoting the Pauli-X and Y operator defined nontrivially on ith and jth qubit. ECR gate is indeed equivalent to the CNOT gate up to some single qubit rotations.

In Fig. 23, we show the decay of conditional state purity in our noisy simulation. Due to increasing number of gates in the noisy circuit, the purity of the post-measurement conditional state deviates from the ideal unity and undergo an approximately linear decay. Within the 15 steps we simulated, the purity of conditional state remains $\gtrsim 0.75$, indicating the coherence of qubits is remained in our circuit of simulation.